

University of Groningen

The SAURON project - VI. Line strength maps of 48 elliptical and lenticular galaxies

Kuntschner, Harald; Emsellem, Eric; Bacon, R.; Bureau, M.; Cappellari, Michele; Davies, Roger L.; de Zeeuw, P. T.; Falcon-Barroso, Jesus; Krajnovic, Davor; McDermid, Richard M.

Published in:
Monthly Notices of the Royal Astronomical Society

DOI:
[10.1111/j.1365-2966.2006.10153.x](https://doi.org/10.1111/j.1365-2966.2006.10153.x)

IMPORTANT NOTE: You are advised to consult the publisher's version (publisher's PDF) if you wish to cite from it. Please check the document version below.

Document Version
Publisher's PDF, also known as Version of record

Publication date:
2006

[Link to publication in University of Groningen/UMCG research database](#)

Citation for published version (APA):

Kuntschner, H., Emsellem, E., Bacon, R., Bureau, M., Cappellari, M., Davies, R. L., de Zeeuw, P. T., Falcon-Barroso, J., Krajnovic, D., McDermid, R. M., Peletier, R. F., & Sarzi, M. (2006). The SAURON project - VI. Line strength maps of 48 elliptical and lenticular galaxies. *Monthly Notices of the Royal Astronomical Society*, 369(2), 497-528. <https://doi.org/10.1111/j.1365-2966.2006.10153.x>

Copyright

Other than for strictly personal use, it is not permitted to download or to forward/distribute the text or part of it without the consent of the author(s) and/or copyright holder(s), unless the work is under an open content license (like Creative Commons).

The publication may also be distributed here under the terms of Article 25fa of the Dutch Copyright Act, indicated by the "Taverne" license. More information can be found on the University of Groningen website: <https://www.rug.nl/library/open-access/self-archiving-pure/taverne-amendment>.

Take-down policy

If you believe that this document breaches copyright please contact us providing details, and we will remove access to the work immediately and investigate your claim.

Downloaded from the University of Groningen/UMCG research database (Pure): <http://www.rug.nl/research/portal>. For technical reasons the number of authors shown on this cover page is limited to 10 maximum.

The SAURON project – VI. Line strength maps of 48 elliptical and lenticular galaxies

Harald Kuntschner,^{1*} Eric Emsellem,² R. Bacon,² M. Bureau,³ Michele Cappellari,⁴ Roger L. Davies,³ P. T. de Zeeuw,⁴ Jesús Falcón-Barroso,⁴ Davor Krajnović,³ Richard M. McDermid,⁴ Reynier F. Peletier⁵ and Marc Sarzi^{3,6}

¹*Space Telescope European Coordinating Facility, European Southern Observatory, Karl-Schwarzschild-Str. 2, 85748 Garching, Germany*

²*CRAL-Observatoire, 9 Avenue Charles-André, 69230 Saint-Genis-Laval, France*

³*Denys Wilkinson Building, University of Oxford, Keble Road, Oxford*

⁴*Leiden Observatory, Postbus 9513, 2300 RA Leiden, the Netherlands*

⁵*Kapteyn Astronomical Institute, Postbus 800, 9700 AV Groningen, the Netherlands*

⁶*Centre for Astrophysics Research, University of Hertfordshire, Hatfield, Herts AL10 9AB*

Accepted 2006 January 30. Received 2006 January 23; in original form 2005 September 11

ABSTRACT

We present absorption line strength maps of 48 representative elliptical and lenticular galaxies obtained as part of a survey of nearby galaxies using our custom-built integral-field spectrograph, SAURON, operating on the William Herschel Telescope. Using high-quality spectra, spatially binned to a constant signal-to-noise ratio, we measure four key age, metallicity and abundance ratio sensitive indices from the Lick/IDS system over a two-dimensional field extending up to approximately one effective radius. A discussion of calibrations and offsets is given, along with a description of error estimation and nebular emission correction. We modify the classical Fe5270 index to define a new index, Fe5270_S, which maximizes the useable spatial coverage of SAURON. Maps of H β , Fe5015, Mg *b* and Fe5270_S are presented for each galaxy. We use the maps to compute average line strengths integrated over circular apertures of one-eighth effective radius, and compare the resulting relations of index versus velocity dispersion with previous long-slit work. The metal line strength maps show generally negative gradients with increasing radius roughly consistent with the morphology of the light profiles. Remarkable deviations from this general trend exist, particularly the Mg *b* isosurface contours appear to be flatter than the isophotes of the surface brightness for about 40 per cent of our galaxies without significant dust features. Generally, these galaxies exhibit significant rotation. We infer from this that the fast-rotating component features a higher metallicity and/or an increased Mg/Fe ratio as compared to the galaxy as a whole. The H β maps are typically flat or show a mild positive outwards radial gradient, while a few galaxies show strong central peaks and/or elevated overall H β strength likely connected to recent star formation activity. For the most prominent post-starburst galaxies, even the metal line strength maps show a reversed gradient.

Key words: galaxies: bulges – galaxies: elliptical and lenticular, cD – galaxies: evolution – galaxies: formation – galaxies: kinematics and dynamics – galaxies: structure.

1 INTRODUCTION

We are carrying out a survey of the dynamics and stellar populations of 72 representative nearby early-type galaxies and spiral bulges based on measurements of the two-dimensional kinematics and line strengths of stars and gas with SAURON, a custom-built panoramic

integral-field spectrograph for the William Herschel Telescope, La Palma (Bacon et al. 2001, hereafter Paper I). The goals and objectives of the SAURON survey are described in de Zeeuw et al. (2002, hereafter Paper II), which also presents the definition of the sample. The full maps of the stellar kinematics for the 48 elliptical (E) and lenticular (S0) galaxies are given in Emsellem et al. (2004, hereafter Paper III). The morphology and kinematics of the ionized gas emission are presented in Sarzi et al. (2006, hereafter Paper V). The stellar and gaseous kinematics of the spiral bulges are described in

*E-mail: hkuntsch@eso.org

Falcón-Barroso et al. (2006). Here, we present maps of the absorption line strength measurements for the 48 E and S0 galaxies in the survey. The analysis of the line strength maps, and a full analysis of the spiral galaxies in the sample will be presented in later papers of this series. The data and maps presented here will be made available via the SAURON web page <http://www.strw.leidenuniv.nl/sauron/>.

The measurement of absorption line strengths in combination with stellar population models has been used for many years to probe the luminosity-weighted age, metallicity and abundance ratios of certain elements in integrated stellar populations (e.g. Faber 1973; Burstein et al. 1984; Rose 1985; Brodie & Hanes 1986; Bica, Alloin & Schmidt 1990; Davies, Sadler & Peletier 1993; González 1993; Worthey 1994; Vazdekis 1999; Thomas, Maraston & Bender 2003). Integral-field spectroscopy allows to obtain spectroscopic information over a contiguous area on the sky and thus to identify two-dimensional structures (see e.g. Emsellem et al. 1996; Peletier et al. 1999; del Burgo et al. 2001). For the first time, we can apply this technique to absorption line strength observations in a large representative sample of early-type galaxies.

One of the most widely used methods for investigating the optical spectra of old (age ≥ 1 Gyr) integrated stellar populations in early-type galaxies is to derive line strength indices in the Lick/IDS system (Burstein et al. 1984; Worthey et al. 1994; Trager et al. 1998), and compare them with stellar population models. We adopt this system in order to allow comparison with existing data. For future analysis, we envisage the use of higher resolution line strength systems once they become available.

In this paper, we present the SAURON line strength measurements for our 48 representative E and S0 galaxies, together with a brief analysis which focuses on the overall characteristics of the maps. A full stellar population analysis of the line strength maps with the help of stellar population models will be presented in a future paper in this series.

This paper is organized as follows. In Section 2, we summarize our observational campaign, while the data reduction steps are outlined in Section 3 along with a discussion on the flux calibration of the data. In Section 4, we describe the definition and measurement of the line strength indices. The two-dimensional line strength maps are presented in Section 5, while in Section 6 we discuss line strength gradients and aperture corrections. In Section 7, we discuss average line strength measurements extracted from circular apertures of one-eighth effective radius, respectively, and compare them to the literature. The conclusions follow in Section 8. We comment on individual galaxies in Appendix A.

2 OBSERVATIONS

The SAURON survey of 72 galaxies was carried out during eight observing runs over 4 yr (56 observing nights allocated). Details on the observing conditions, instrument set-up and exposure times are given in Paper III. The SAURON sample of 48 E and S0 galaxies is representative of nearby bright early-type galaxies ($cz \leq 3000 \text{ km s}^{-1}$; $M_B \leq -18 \text{ mag}$). As discussed in Paper II, it contains 24 galaxies in each of the E and S0 subclasses, equally divided between ‘field’ and ‘cluster’ objects (the latter defined as belonging to the Virgo cluster, the Coma I cloud and the Leo I group), uniformly covering the plane of ellipticity ϵ versus absolute blue magnitude M_B . Tables A1 and A2 in Paper II provide basic information on the objects.

The SAURON survey is carried out with the low-resolution mode of the instrument, giving a field of view (FoV) of $33 \times 41 \text{ arcsec}^2$, contiguously sampled by $1431 \text{ } 0.94 \times 0.94 \text{ arcsec}^2$ lenses, each

Table 1. List of spectrophotometric standard stars.

Name (1)	Run observed (2)	Calibration (3)
Feige 34	5, 6, 7	STIS+Oke
Feige 66	1, 3	FOS+Oke
G191B2B	1, 4, 5, 6	Model
HZ44	1, 3	STIS
BD+28 4211	2, 4	STIS
BD+33 2642	7	FOS+Oke
HD 09352	5	STIS
EG 131	4, 5, 7	–

Notes. Listed are the spectrophotometric standard stars which were used to establish the flux calibration curve for the SAURON system. Column 1 lists the name of the star while Column 2 gives the run where the star was observed (see Paper III). Column 3 denotes the type of calibration file which was used for the absolute flux calibration (see Bohlin et al. 2001, for details). The star EG 131 is a special continuum correction star. See text for details.

of which produces a spectrum. Another 146 lenses sample a small region 1.9 arcmin from the field centre, which are used for simultaneous sky subtraction. The spectral resolution of the observed wavelength range $4800\text{--}5380 \text{ \AA}$ is $\sim 4.2 \text{ \AA}$ [full width at half-maximum (FWHM), $\sigma_{\text{inst}} \simeq 108 \text{ km s}^{-1}$] and sampled at $1.1 \text{ \AA pixel}^{-1}$. This wavelength range includes a set of potential emission lines (e.g. $H\beta$, $[O III]$, $[N I]$) and stellar absorption lines (e.g. $H\beta$, Mg , Fe) which can be used to investigate the stellar populations.

Each galaxy field was typically exposed for $4 \times 1800 \text{ s}$, dithered by about 1 arcsec. In 30 per cent of the cases, we constructed mosaics of two or three pointings to cover the galaxy out to about one effective radius R_e , or, for the largest objects, out to $\sim 0.5 R_e$. The footprints of these pointings are shown overlaid on a Digital Sky-Survey image in fig. 1 of Paper III.

In order to allow for inter-run calibration and provide templates for redshift and velocity dispersion measurements, we observed during each run a number of stars covering a broad range of spectral types. Specifically, we included stars from the Lick stellar library catalogue (Worthey et al. 1994) in order to calibrate our line strength measurements to the Lick/IDS system and its associated models (e.g. Worthey 1994, see also Section 4.2.3). Spectrophotometric standard stars were also observed to calibrate the response function of the system (see Table 1).

3 DATA REDUCTION

We reduced the SAURON observations with the dedicated XSAURON software developed at CRAL-Observatoire, and described in Paper I. The basic reduction steps include bias and dark subtraction, extraction of the spectra using a fitted mask model, wavelength calibration, low-frequency flat-fielding, cosmic-ray removal, homogenization of the spectral resolution, sky subtraction and flux calibration. The wavelength calibration is accurate to 0.1 \AA (6 km s^{-1} , rms).

Multiple exposures of the same galaxy were merged and mosaiced together. In this process, the wavelength domain was truncated to a common range and the data cubes resampled to a spatial scale of $0.8 \times 0.8 \text{ arcsec}^2$ with orientation north up and east to the left. In order to allow for a meaningful analysis, the final data cubes were spatially binned to a minimum signal-to-noise ratio (S/N) of 60 per \AA using an adaptive scheme developed by (Cappellari & Copin

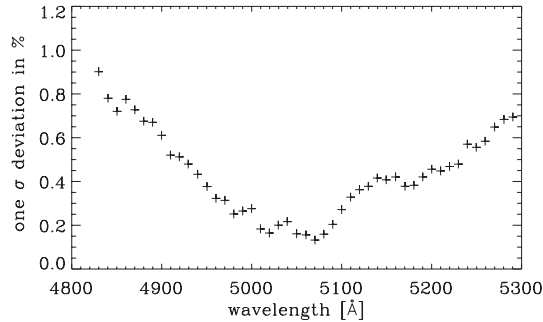


Figure 1. 1σ standard deviation of the spectral response function between our seven observing runs as a function of wavelength. The 22 stellar observations used for this analysis were normalized in a 100-Å region at 5060 Å. The evaluation of the scatter was performed in ~ 10 -Å steps.

2003). In this approach, the spectra are co-added by starting from the highest S/N lenslet, and accreting additional lenslets closest to the current bin centroid. A new bin is started each time the target S/N is reached. The resulting bin centroids are then used as starting points for a centroidal Voronoi tessellation, ensuring compact non-overlapping bins and a uniform S/N in faint regions. The binning used in this paper is identical to the one used in Papers III and V.

In the following, we describe in more detail how the flux calibration was derived, since this is an important issue for the derivation of line strength indices which was not covered in detail in previous papers of this series. We also summarize the removal of emission lines which is another important step before the measurement of absorption line strength.

3.1 Flux calibration

3.1.1 Overall flux calibration

During each observing run, a number of spectrophotometric standards were observed, typically close to the centre of the FoV of SAURON (see Table 1). As a first step, we evaluated the inter-run consistency of the spectral response function of SAURON. For this purpose, we investigated the relative changes in the spectral response function in repeat observations of six flux standard stars. In this analysis, we are only interested in the relative changes, so we eliminated the overall throughput difference by normalizing each set of observations of the same star in a 100-Å region in the middle of the wavelength range. In total, 22 repeat observations¹ were used.

The results are presented in Fig. 1. The relative run-to-run deviations in spectral response are smaller than 1 per cent (1σ standard deviation) over the full wavelength range. An analysis of the variations in *absolute* throughput for 13 standard stars observed in photometric nights during the survey gives a standard deviation of 5 per cent. No significant run-to-run variations could be established. Since the overall stability of the instrument is satisfactory, we adopt a common flux calibration curve for all runs which is described in the following.

In order to establish an absolute flux calibration for our spectra, a two-step procedure was adopted. (i) A relative spectral response function was established which maps throughput variations on ~ 100 -Å scales introduced by a wavelength selection filter in

¹Note that some flux standard stars were observed multiple times within one run.

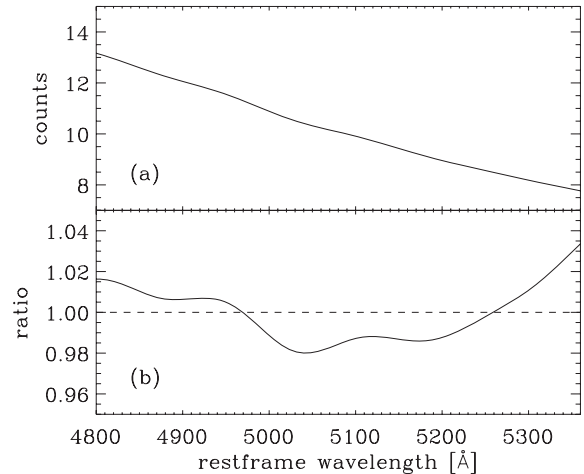


Figure 2. (a) The flux calibration curve for the SAURON survey normalized to arbitrary units. (b) Small-scale variations of the flux calibration curve after the removal of a linear fit.

the instrument (see Paper I). (ii) The flux calibration tables compiled by Bohlin, Dickinson & Calzetti (2001, ‘CALSPEC’ directory) were used to establish an absolute calibration of the SAURON system.

The first step in the calibration procedure is necessary since small-scale variations cannot easily be removed by the coarse wavelength steps of classical flux calibration tables. Furthermore, it is not uncommon to find large residuals at the position of absorption features (e.g. H β). To overcome these problems, we observed in runs 4, 5 & 7 the white dwarf EG 131 (see Paper III). This star shows an exceptionally smooth continuum over the SAURON wavelength range, and in particular does not show any notable H β absorption (M. Bessel, private communication). This makes it an ideal calibration star to remove small-scale continuum variations. Unfortunately, there is no absolute flux calibration available for EG 131, but the energy distribution of a blackbody with a temperature of $\sim 11\,800$ K can be used to define the continuum (M. Bessel, private communication).

Fig. 2 shows the result from our analysis of the flux standard stars. We find several ‘wiggles’ with a peak-to-peak amplitude of up to 3 per cent. These wiggles, primarily derived from the observations of EG 131, can be confirmed in an independent way with the standard star G191B2B since Bohlin et al. (2001) provide a model flux calibration curve at a similar resolution as the SAURON observations. This model flux curve is of very high quality and provides accurate flux values even at small wavelength intervals. Both standard stars, EG 131 and G191B2B, give consistent results. In order to establish the absolute flux calibration curve for the SAURON survey, we used all flux standard stars listed in Table 1 and the corresponding flux tables given in Bohlin et al. (2001).

Before applying the overall flux calibration curve to our data, the observed spectrum is corrected for air mass according to the average extinction curve for La Palma (King 1985). The spectra are not corrected for Galactic extinction since the correction would be negligible over the observed wavelength range.

Although we derive from the photometric standard star observations a very stable behaviour of the instrument and a well-calibrated flux curve, we cannot directly transfer this conclusion to the full data set. For example, variations as a function of FoV and sky-subtraction errors for low S/N regions can have a significant effect on the flux calibration accuracy.

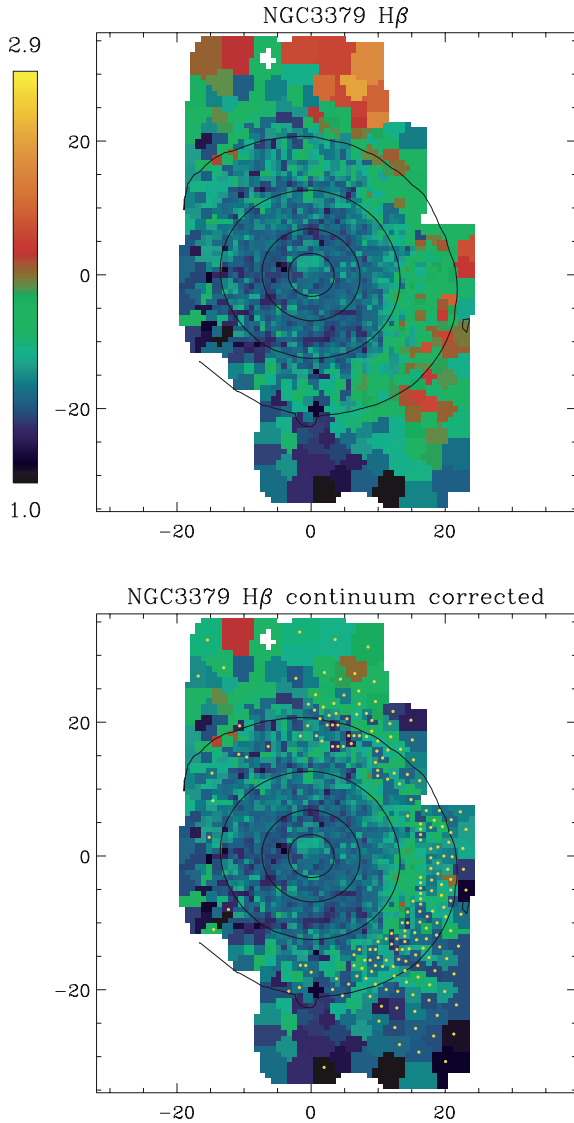


Figure 3. The $H\beta$ map of NGC 3379 before (top plot) and after (bottom plot) continuum correction. The range in $H\beta$ strength is indicated by the colour bar, and the numbers to the top and bottom of the colour bar give the range in $H\beta$ [Å]. The scale is the same for both plots. The yellow dots in the bottom plot indicate all bins which were corrected for the continuum variation. North is up and east to the left. The spatial axis are given in arcsec.

3.1.2 Continuum correction for line strength indices

An analysis of our $H\beta$ line strength measurements showed that we find non-physically strong absorption strengths in the outer bins of some galaxies often at the right-hand side (as shown in Fig. 3) of the FoV. A closer inspection revealed that the abnormal $H\beta$ absorption strength is mainly caused by a wrong continuum shape across the $H\beta$ region. In the outer bins, typically many individual lenslets need to be summed up in order to reach our minimum target S/N of 60. Therefore, any systematic errors, such as imperfect tracing of the spectra on the CCD or sky subtraction, will be present in the final binned spectrum. Unfortunately, we were unable to remove these errors in our data reduction, and thus decided to correct the continuum in the binned spectrum.

In order to obtain a good template spectrum for each galaxy, we derive the optimal template for an average spectrum, within a

10-arcsec radius, of each galaxy. This optimal template is the weighted combination of 19 spectra, spanning a range in age and metallicity, from the library of stellar population models of Vazdekis (1999), and additionally six spectra from the Jones (1997) stellar library from which the Vazdekis models are built to provide spectra with large Mg absorption strengths (for details see Paper III). The optimal template is obtained from an emission line corrected (see Section 3.2) average spectrum by simultaneously fitting the stellar kinematics together with the templates, and using a low-order polynomial.

For each individual bin of the galaxy in question, we fit this optimal template, with the kinematics fixed to the values of Paper III, together with an 11th order multiplicative polynomial continuum over the full wavelength range of the spectrum. Then in a second step, we check if the continuum fit shows significant second and higher order structure over the wavelength range of the $H\beta$ index. Linear continuum variation does not affect the measured line strengths. Only for bins covering more than one lenslet and where we detect a significant² continuum variation, we divide by the continuum fit and thus apply the continuum correction before measuring the $H\beta$ index. All bins which have been continuum corrected show a flag in the data cubes of the public release, and, furthermore, we added (in quadrature) a constant systematic error of 0.1 Å to the $H\beta$ index of corrected bins. The typical fraction of corrected bins in a data cube is 4 per cent, while the extremes go from 1 to 33 per cent. As an example, Fig. 3 shows the full $H\beta$ map of NGC 3379 before and after the continuum correction.

In Fig. 4, we show a simulated long-slit observation of the $H\beta$ absorption strength along the major axis of NGC 3379 derived from the SAURON data before and after the continuum correction. The top panel clearly shows the points at large negative radii where the continuum has been corrected. The literature comparison (bottom panel) shows a good agreement.

The success of our continuum correction is critically dependent on the ability of the optimal template to fit the observed spectrum. In general, this may be a problem if the galaxy shows non-solar abundance ratios which are not mimicked by the template library. However, in the case of $H\beta$ the index is only weakly dependent on abundance ratio (Trager et al. 2000; Thomas et al. 2003) and thus the method works well. Continuum variations can in principle also affect other indices, such as Fe5015 and Mg *b*. Maps of Fe5015 are clearly affected, while Mg *b* maps show evidence of continuum problems for only a handful of galaxies. For metal indices, abundance ratios are a critical issue. The continuum variations and unaccounted abundance ratio differences between the galaxy spectrum and the optimal template are largely degenerate (at least for our data and models). Thus, we decided not to correct the Fe5015, Mg *b* and Fe5270_s indices. For selected galaxies, we remove bins which suffer from significant continuum problems (see also Section 5).

3.2 Emission-line corrections

Many early-type galaxies show signs of relatively weak emission from ionized gas and dust in the interstellar medium (e.g. Goudfrooij et al. 1994). Three out of four of the main absorption line features in the SAURON wavelength range are potentially affected by emission lines; namely $H\beta$, [O III]λ4959, [O III]λ5007 and [N I]λ5200. Before measuring *absorption line* indices, these emission lines,

²The rms deviations are greater than 0.006 after the removal of a straight line fit.

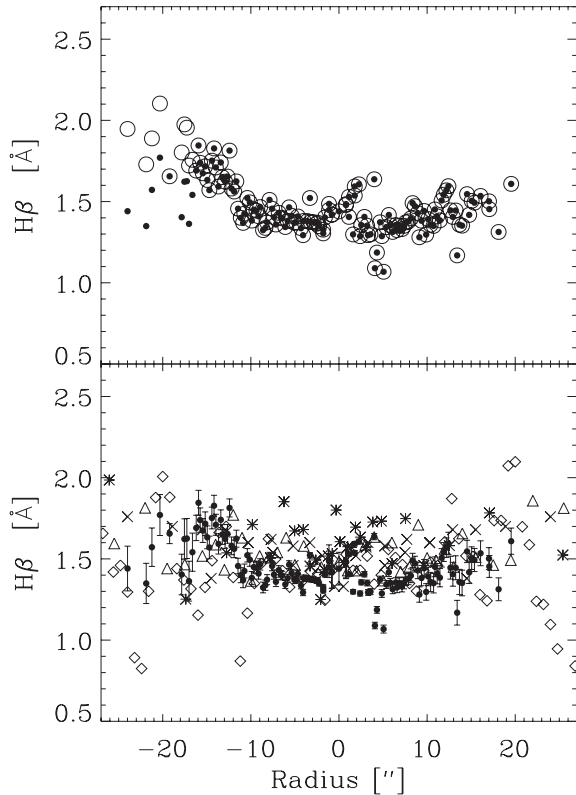


Figure 4. Effects of continuum correction for NGC 3379 (major axis). The top plot shows SAURON data before (open circles) and after (filled circles) continuum correction for the $H\beta$ index. The bottom panel shows a comparison with literature data. Error bars are only plotted for the SAURON data. The data of Davies et al. (1993) are shown as crosses and mirrored about the zero point; data from González (1993, and private communication) are shown as open triangles; the data of McDermid et al. (2005) are shown as stars. Sánchez-Blázquez (2004) observations are shown as open diamonds. Literature data outside ± 27 arcsec are not shown.

where present, need to be removed taking into account that the gas kinematics can be decoupled from the stellar kinematics. This is done as part of our efforts to analyse the emission lines themselves. The emission-line measurements and results are described in detail in Paper V. Here we give only a short summary.

For five galaxies, we find no emission above our detection limit (NGC 821, 2695, 4387, 4564 and 5308); for a further seven galaxies we find only weak evidence for emission (NGC 4270, 4382, 4458, 4473, 4621, 4660 and 5845), while all of the remaining galaxies in our survey show clear signs of emission. All emission lines are modelled with a simple Gaussian profile. Using the stellar kinematics derived in Paper III, we re-derive the best fitting, optimal stellar template³ in combination with the best-fitting emission template featuring [O III] only. While the [O III] strengths and kinematics are free parameters in this first step, the regions of potential $H\beta$ and [N I] emission are masked. If no significant [O III] emission is found, we assume that there is also no $H\beta$ and [N I]. This limits our ability

to measure weak emission associated with star formation regions where $H\beta/[O III] \gg 1$. This is an unavoidable consequence of the fact that *weak* $H\beta$ emission cannot always reliably be measured without constraining its kinematics. Whether emission is found or not is determined by a measure of the amplitude of the emission lines with respect to the level of both statistical and systematic deviations from the fit to the stellar continuum. As a cut-off, we use an amplitude-over-noise (hereafter A/N) ratio of 4. This corresponds to a detection limit of 0.1 \AA in the central, high S/N, parts of the line strength maps and is reduced to approximately 0.2 \AA in the outer parts.

If we find significant [O III] emission, we re-fit the galaxy spectrum allowing for potential $H\beta$ and [N I] emission. For galaxies with weak emission lines, we constrain the $H\beta$ and [N I] emission kinematics to be the same as the [O III] ones. For 10 galaxies (NGC 2768, 3032, 3414, 4278, 4374, 4459, 4486, 4526, 5838 and 5846) with relatively strong emission, we are able to fit the $H\beta$ emission kinematics independently, while the [N I] kinematics are tied to $H\beta$ (see Paper V for details). The A/N detection limits for $H\beta$ is set to 3 and 5 for the constrained and unconstrained kinematics, respectively. The detection limits for $H\beta$ emission are 0.06 and 0.2 \AA in the inner and outer parts of the galaxies, respectively.

For [N I], the A/N detection limit is always set to 4. We note that especially for the [N I] emission line the dominating source of noise is not shot noise from the spectrum, but template mismatch due to unaccounted for non-solar abundance ratios in the galaxies. We therefore measure the A/N for the [N I] emission line in the Mg *b* region which is a good guide for the degree of template mismatch. Due to the difficulty of quantifying the effects of template mismatch, the detection limits of the [N I] line are not well established. They will be, however, similar to the [O III] detection limits and somewhat larger for objects with large non-solar abundance ratios.

In Fig. 5, we show an example map for the emission correction of the $H\beta$ feature. NGC 4526 has an inclined dust disc in the central $20 \times 20 \text{ arcsec}^2$ (see Paper V) showing very regular gas kinematics and a circumnuclear region with particularly strong $H\beta$ emission. After emission correction, a relatively thin elongated region of strong $H\beta$ absorption coinciding with the dust disc appears. This example is representative of the strongest emission corrections in our data.

Many previous authors corrected for $H\beta$ emission using an average ratio between the [O III] $\lambda 5007$ and $H\beta$ lines. For instance, Trager et al. (2000) concluded that 0.6 times the [O III] $\lambda 5007$ emission is a reasonable estimate for the $H\beta$ emission. However, in their sample of 27 galaxies the correction factor varies from 0.33 to 1.25 , and it is therefore doubtful whether this correction is accurate for an individual galaxy (see also Mehlert et al. 2000). We confirm this with our data (see Fig. 6) and find a median correction factor of 0.67 with a range from 0.3 to 2.3 . There is weak evidence that the average correction factor is a function of emission strength, becoming smaller at large [O III] $\lambda 5007$ strength. More importantly, we point out that emission-line ratios generally vary significantly across the galaxies (see error bar in Fig. 6 and [O III]/ $H\beta$ maps in Paper V). NGC 3032 shows an exceptionally large ratio of $H\beta/[O III] \simeq 2.1$, pointing towards ongoing star formation over a significant area of the galaxy.

4 THE LINE STRENGTH MEASUREMENTS

Here, we describe which line strength indices we use for the SAURON survey, the calibration of our measurements to the standard Lick/IDS system and the evaluation of the line strength errors.

³The composition of the template library was improved with respect to the one used in Paper III. Three stars from the Jones (1997) library were exchanged with more suitable ones which allowed a better match of the spectral characteristics in large early-type galaxies and thus an improved emission correction. The effects on the derivation of the stellar kinematics are negligible.

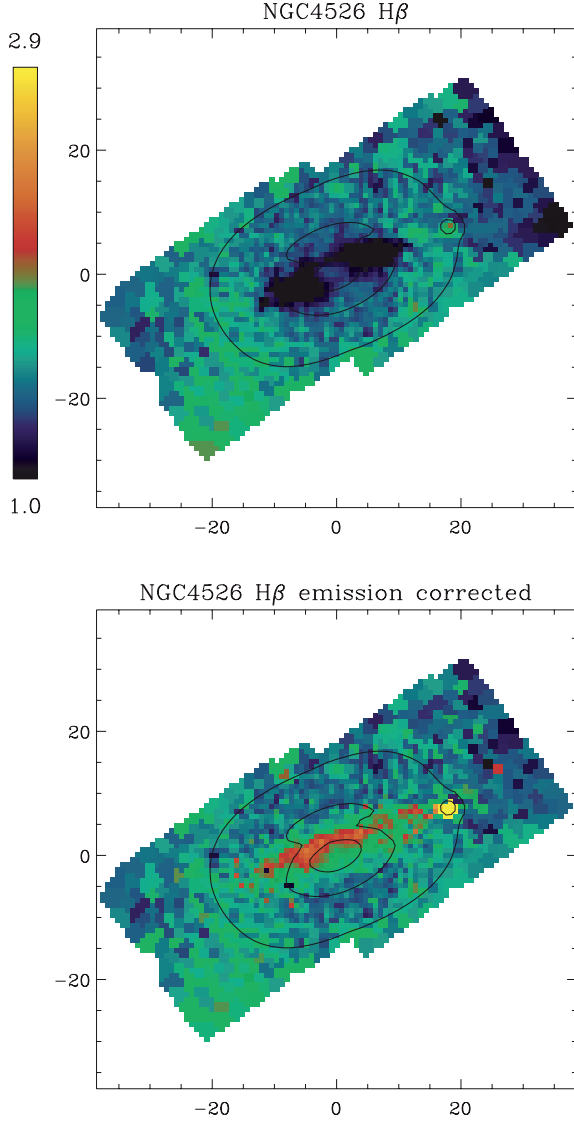


Figure 5. The $H\beta$ map of NGC 4526 before (top plot) and after (bottom plot) emission and continuum correction. The range in $H\beta$ strength is indicated by the colour bar, and the numbers to the top and bottom of the colour bar give the range in $H\beta$ [Å]. The scale is the same for both plots. North is up and east to the left. The spatial axis is given in arcsec. The small circular region of strong $H\beta$ absorption visible in both maps (RA \simeq 18 arcsec and Dec. \simeq 7 arcsec) corresponds to the position of a star in the FoV.

4.1 Line strength indices

In the Lick/IDS system, absorption line strengths are measured by indices, where a central feature bandpass is flanked to the blue and red by pseudo-continuum bandpasses (see Fig. 7). The mean height in each of the two pseudo-continuum regions is determined on either side of the feature bandpass, and a straight line is drawn through the midpoint of each one. The difference in flux between this line and the observed spectrum within the feature bandpass determines the index (Trager et al. 1998). For most absorption features, the indices are expressed in angstroms of equivalent widths.⁴

⁴For broad molecular bands, the index is expressed in magnitudes. No such indices are used in the SAURON system.

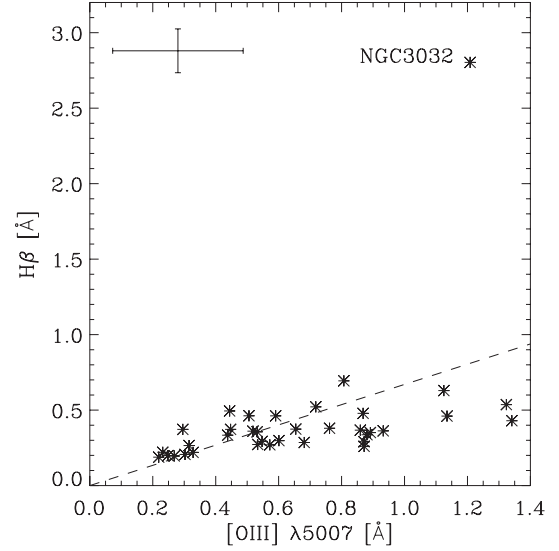


Figure 6. Median $H\beta$ emission versus $[O\text{ III}]\lambda 5007$ for all galaxies with significant detection of emission lines. The error bar in the top left corner shows a typical range of emission strength found *within* individual galaxies (estimated as a robust 1σ standard deviation). The dashed line reflects the relation of $H\beta = 0.67 \times [O\text{ III}]\lambda 5007$ corresponding to our median correction factor. The position of NGC 3032 is indicated by its name; for details see text.

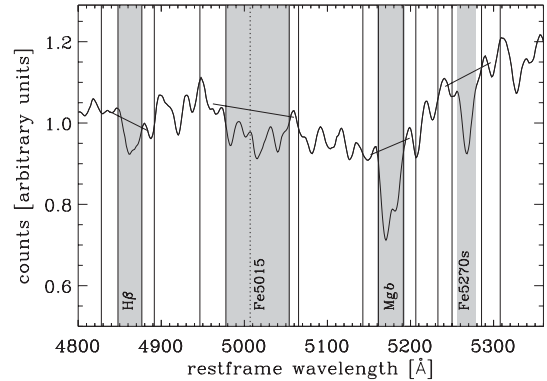


Figure 7. The set of line strength indices shown on a central SAURON spectrum of NGC 3379. The shaded regions are the central bandpasses, whereas the dashed lines indicate the side-bandpasses. The solid lines show the pseudo-continuum determined from the side-bandpasses. The location of the $[O\text{ III}]\lambda 5007$ emission line is indicated by the dotted line.

The exact wavelength definitions of the indices, the observed wavelength range and the redshift of the object determine which indices can be measured. The full wavelength range of SAURON is 4760–5400 Å. However, the tilting of the wavelength selection filter in order to avoid ghost images reduces the useable wavelength range common to all lenslets to approximately 4825–5275 Å (see Paper I). For the nearby sample of SAURON galaxies (i.e. $cz \leq 3000$ km s^{−1}), this wavelength range allows us to measure three Lick/IDS indices: $H\beta$, Fe5015 and Mg b (see Table 2).

The useable wavelength range is a well-determined function of position on the CCD. The red wavelength limit is most affected, and varies from 5275 to 5380 Å over the FoV. For lenslets with a red-extended wavelength coverage, we can measure a further Lick/IDS index: Fe5270. It is desirable to measure this index since it is an

Table 2. Bandpass definitions of SAURON line strength indices.

Index	Blue pseudo-continuum	Central bandpass	Red pseudo-continuum	Units	Source
H β	4827.875–4847.875	4847.875–4876.625	4876.625–4891.625	Å	Trager et al. (1998)
Fe5015	4946.500–4977.750	4977.750–5054.000	5054.000–5065.250	Å	Trager et al. (1998)
Mg <i>b</i>	5142.625–5161.375	5160.125–5192.625	5191.375–5206.375	Å	Trager et al. (1998)
Fe5270	5233.150–5248.150	5245.650–5285.650	5285.650–5318.150	Å	Trager et al. (1998)
Fe5270 _S	5233.000–5250.000	5256.500–5278.500	5285.500–5308.000	Å	This paper

important ingredient to investigate the Mg-to-Fe abundance ratios in integrated stellar populations (Worthey, Faber & Gonzalez 1992).

Since the red wavelength cut-off is a monotonic function across the FoV, by making the red bandpass of the Fe5270 index as blue as possible, we effectively increase the useable FoV. For this reason, we have designed a new index for the Fe5270 absorption feature with a reduced red wavelength coverage. The bandpass definitions of all indices used for the SAURON survey are summarized in Table 2.

The main aim of the re-definition of the Fe5270 index is to increase the effective FoV. A useful re-definition of the index should also, however, obey the following conditions: (i) small and well-determined line-of-sight-velocity-distribution (hereafter LOSVD) corrections (see Section 4.2.2); (ii) good Poisson statistics; (iii) similar sensitivity towards changes in age, metallicity and abundance ratios as the original Lick/IDS Fe5270 index in order to allow easy conversion.

In order to evaluate the optimal new index definition, we first created a catalogue of model spectra resembling typical SAURON observations of early-type galaxies. In fact, we employed the same model spectra library as used for the optimal template determination (see Paper III) and the LOSVD corrections (see Section 4.2.2). By using this model library, we cover the range of expected observations for the Fe5270 absorption feature reasonably well.

All six wavelength values (see Table 2) which define an index were systematically changed in 0.5-Å steps until an optimal definition⁵ was found. The bluest wavelength definition of the red pseudo-continuum which still gives reasonable LOSVD corrections and error statistics for the index turns out to be 5308.0 Å. This is a reduction of ≈ 10 Å in the red-most limit of the original Lick/IDS definition, equivalent to an increase in the FoV of 13 per cent.

The LOSVD correction for a purely Gaussian LOSVD for the new index is only 5.1 per cent at 200 km s⁻¹ as compared to 10.3 per cent for the original index. While the index could be improved in terms of its velocity dispersion corrections and Poisson statistics, it also shows a good linear relation with the original Lick/IDS index, i.e. it shows a similar dependence on age and metallicity (see Fig. 8). Fortunately, the re-definition of this index did not significantly change its overall sensitivity to abundance ratios (Korn, Maraston & Thomas 2005). The best-fitting linear relation determined from stellar population models of Vazdekis (1999) with ages ≥ 4 Gyr is

$$\text{Fe5270} = 1.26 \times \text{Fe5270}_S + 0.06. \quad (1)$$

The formal errors of the fit are smaller than ± 0.01 . In this paper, we use the above equation to convert our Fe5270_S measurements to the

⁵The index definition was optimized at the instrumental resolution of SAURON (≈ 108 km s⁻¹) in order to allow for the new generation of stellar population models which will be able to make predictions at this spectral resolution.

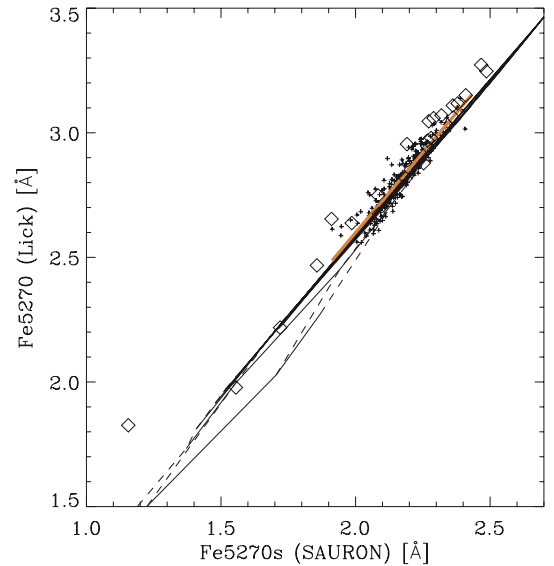


Figure 8. The relation between the new Fe5270_S index and the original Lick/IDS index Fe5270. The small plus signs represent SAURON observations of NGC 3379 within an 8-arcsec radius of the centre, while the open diamonds show the central measurements of a complete sample of early-type galaxies in the Fornax cluster (Kuntschner 2000). The thick solid red line is a linear fit to the SAURON data: $\text{Fe5270} = 1.28 \times \text{Fe5270}_S + 0.03$. Overplotted are model predictions by Vazdekis (1999) at the Lick/IDS resolution.

Lick Fe5270 index. We note, an empirically determined conversion formula compares well ($\text{Fe5270} = 1.28 \times \text{Fe5270}_S + 0.03$; see Fig. 8).

In order to maximize the information for the line strength indices, we produce for each galaxy two data cubes: one containing the H β , Fe5015 and Mg *b* indices for the full FoV and one presenting the new Fe5270_S index for a reduced FoV. Due to the adaptive two-dimensional binning, the final spatial sampling of the two data cubes is not identical.

4.2 Calibration to the Lick/IDS system

In order to allow a meaningful comparison between stellar population model predictions and observed data, the index measurements need to be carefully calibrated to the Lick/IDS system. There are three effects to account for: (i) the difference in the spectral resolution between the Lick/IDS system and the SAURON instrumental set-up; (ii) the internal velocity broadening of the observed objects and (iii) small systematic offsets caused by continuum shape differences (Worthey & Ottaviani 1997; Kuntschner 2000).

In the following paragraphs, we describe the individual steps taken to ensure an accurate calibration of the SAURON data to the Lick/IDS system.

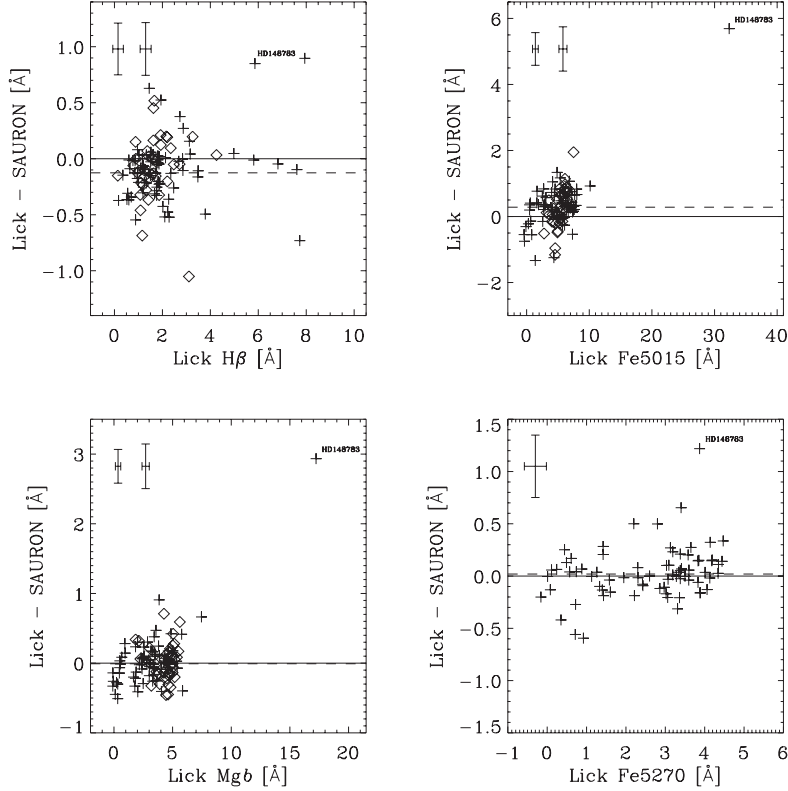


Figure 9. Comparison of Lick/IDS and our measurements for 73 stars in common (plus signs). For one star (HD 148783, spectral type M6III), our measurements were drastically different for all four indices. The dashed line shows the mean offset derived by a biweight estimator (see also Table 3). Observations of galaxies in common between Lick and SAURON are shown as open diamonds. A typical error bar for an individual star is shown in the upper left corner of each panel. For the galaxy comparisons, we plot a separate representative error bar. The error is dominated by the observational error of the Lick/IDS data. Note that the stellar observations span very well the index range covered by the galaxies.

4.2.1 Spectral resolution correction

First, we need to adjust for the difference in spectral resolution between the Lick/IDS system and the SAURON observations for line strength measurements. The nominal resolution of the Lick/IDS system in the SAURON wavelength range is 8–9 Å (FWHM) with a mean of 8.4 Å (Worthey & Ottaviani 1997). We degrade our spectra to approximately the Lick/IDS resolution by broadening to an instrumental resolution of $\sigma = 212 \text{ km s}^{-1}$.

4.2.2 LOSVD corrections

The observed spectrum of a galaxy is the convolution of the integrated spectrum of its stellar population(s) by the instrumental broadening and LOSVD of the stars. These effects broaden the spectral features, in general reducing the observed line strength compared to the intrinsic values. In order to compare the index measurements for galaxies with model predictions, we calibrate the indices to zero-velocity dispersion and the nominal Lick/IDS resolution.

In the past, most authors have only taken into account the first moments, v and σ , of the LOSVD to correct the line strength indices. However, with the availability of high-quality measurements of the higher order terms h_3 and h_4 which describe non-Gaussian deviations (see e.g. Paper III), we need to apply more accurate corrections. Typically, a non-zero h_3 term does not affect the Lick indices significantly, but a non-zero h_4 term can have significant effects (Hau 1998; Kuntschner 2004).

In order to determine the corrections for each index, we use the optimal template determined for each spectrum individually during the derivation of the kinematics (for details see Paper III). Generally, this optimal template is a good representation of the galaxy spectrum. For each spectrum, a correction factor, $C_j(\sigma, h_3, h_4)$, is determined such that

$$C_j(\sigma, h_3, h_4) = I_j(\sigma = 0, h_3 = 0, h_4 = 0) / I_j(\sigma, h_3, h_4), \quad (2)$$

where I_j is the index measured from the optimal template convolved to the Lick resolution and additionally convolved with the LOSVD given in brackets. A LOSVD-corrected index is then $I_j^{\text{corr}} = C_j(\sigma, h_3, h_4) \times I_j^{\text{raw}}$.

4.2.3 Lick/IDS offsets

Although we matched the spectral resolution of the Lick system, small systematic offsets of the indices introduced by continuum shape differences are generally present. (Note that the original Lick/IDS spectra are not flux calibrated.) To establish these offsets, we compared our measurements for stars in common with the Lick/IDS stellar library (Worthey et al. 1994). In total, we observed 73 different Lick/IDS stars with 174 repeat observations.⁶

Fig. 9 shows the difference between Lick/IDS measurements and ours, where repeat observations of the same star were averaged. The

⁶Since the stars have only small relative velocities and were typically observed at the centre of the SAURON FoV, we were able to measure the original Lick/IDS index Fe5270 for all stars.

Table 3. Offset estimates to the Lick/IDS system.

Index (1)	Offset (stars) (2)	Offset (galaxies) (3)	Offset (Jones stars) (4)	Applied offsets (5)
H β	$-0.13 \pm 0.03 \text{ \AA}$	$-0.06 \pm 0.04 \text{ \AA}$	$-0.12 \pm 0.02 \text{ \AA}$	$-0.13 \pm 0.05 \text{ \AA}$
Fe5015	$+0.28 \pm 0.05 \text{ \AA}$	$+0.27 \pm 0.09 \text{ \AA}$	$+0.23 \pm 0.04 \text{ \AA}$	$+0.28 \pm 0.05 \text{ \AA}$
Mg <i>b</i>	$-0.01 \pm 0.03 \text{ \AA}$	$+0.01 \pm 0.04 \text{ \AA}$	$-0.08 \pm 0.02 \text{ \AA}$	$+0.00 \pm 0.05 \text{ \AA}$
Fe5270	$+0.02 \pm 0.02 \text{ \AA}$	–	$-0.07 \pm 0.02 \text{ \AA}$	$+0.00 \pm 0.05 \text{ \AA}$

Notes. Column 1 gives the index name, while Columns 2 and 3 give the mean offset (Lick–SAURON) to the Lick/IDS system evaluated from the stars and galaxies in common, respectively. Column 4 shows the offsets derived from the comparison of the Jones (1997) library to the Lick/IDS observations for stars in common. Column 5 shows the final offsets we applied to our data and their mean adopted error.

mean offsets and associated errors for each index are evaluated by a biweight estimator to minimize the influence of outliers and are summarized in Table 3. The formal error in the offset is taken to be the standard error on the mean $\sigma/\sqrt{N_{\text{stars}}}$.

As an independent test of this procedure, we compare the Lick/IDS measurements for the 42 galaxies in common with our survey.⁷ This is more difficult than the similar comparison for stars since for galaxies, e.g. aperture differences and seeing variations can affect the results. In order to match the Lick/IDS standard aperture of $1.4 \times 4 \text{ arcsec}^2$, we extracted the luminosity-weighted mean of a circular aperture with radius $r = 1.335 \text{ arcsec}$ from each line strength map. It would in principle be better to extract the exact Lick aperture: this is however not possible since the position angles of the Lick observations are unknown to us. For this comparison, the SAURON measurements were not corrected for emission but internal line broadening was taken into account (see Section 4.2.2).

The results are overplotted in Fig. 9 as open diamonds and the offsets, evaluated with a biweight estimator, are listed in Table 3. The overall offsets inferred from the galaxies are in good agreement with the offsets derived from the stars. To further test the offsets for Lick indices derived from flux calibrated data, we made use of the Jones (1997) library. First, the data were broadened to the spectral resolution of the Lick/IDS system with a wavelength-dependent Gaussian assuming a constant spectral resolution of $\text{FWHM} = 1.8 \text{ \AA}$ for the Jones stars. Then, we compared the index measurements for the 128 stars in common between the Jones library and the Lick observations (Worthey et al. 1994). The offsets and associated errors, derived with a biweight estimator, are listed in Table 3, Column 4 (see also Norris, Sharples & Kuntschner 2006) and are in good agreement with the offsets derived from the SAURON observations for the H β and Fe5015 indices. The agreement for the Mg *b* and Fe5270 indices is less good, but differences are still small with offsets $< 0.1 \text{ \AA}$. Furthermore, our determination of Lick offsets derived from Jones stars is in excellent agreement with an earlier investigation carried out by (Worthey & Ottaviani 1997, table 9). Although the offsets are small, they can significantly change the age and metallicity estimates. Particularly, the H β index presents a problem, since one can find with the currently available stellar population models age estimates older than the age of the universe if offsets are applied. In the end, we decided to apply Lick offsets only for the H β and Fe5015 indices (see Table 3, Column 5) since all the three offset determination methods give consistent results. For the Mg *b* and

Fe5270 indices, no offsets are applied since the SAURON stellar observations indicate offsets consistent with zero. For all indices, we quote conservative offset errors which reflect the information derived from the stars and galaxies.

4.3 Estimating errors for line strength indices

Several authors have evaluated the sources of errors for line strength indices (Cardiel et al. 1998, and references therein). They can be divided into random and systematic errors. The treatment of systematic errors is generally very difficult, while the random errors can be determined quite accurately. In the following paragraphs, we concentrate on the random errors.

The main ingredients to evaluate the random errors for line strength indices in the SAURON system are the noise spectra which are provided by the data reduction procedure for each individual lenslet (see Paper I). The noise spectrum represents the errors propagated through the full data reduction until the final, merged and binned data cube from which velocities, velocity dispersions, line strength indices, etc. can be determined.

Before measuring a given index on a spectrum, one needs to know (i) the average recession velocity in order to place the index bandpasses correctly and (ii) a measure of the LOSVD in order to correct the index for broadening effects (see Section 4.2.2). Both parameters have associated uncertainties (for details see Paper III) which will contribute to the final index error.

For each galaxy, the random error for each index measurement was estimated via a Monte Carlo approach. For every spatial bin, N realizations of the associated spectrum were produced based on its corresponding noise distribution (assumed to be Gaussian). Likewise, N values of the recession velocity and velocity dispersion were chosen within the uncertainties of their measured values, thus creating a total number of N^3 realizations of the measured index, from which the rms uncertainty was determined. A typical number for N in our analysis was 30. For bins where emission in H β , [O III] or [N I] was detected and subtracted, we add the associated errors in quadrature (see Section 3.2 and Paper V).

Concerning the systematic errors, we consider two main contributions: (i) errors from the continuum correction for the H β line strengths and (ii) the error in the calibration to the Lick system. The continuum correction errors (see Section 3.1.2, assumed to be at a constant level of 0.1 \AA) are added to the affected bins, while the Lick system offsets are quoted in Table 3 and are not added to the individual data points, but are shown as global offset errors in figures.

⁷In the Lick/IDS survey, the Mg *b*, Fe5015 and H β indices are not available for one, three and two galaxies, respectively.

5 OBSERVED LINE STRENGTH MAPS

Figs 10(a)–(l) below present maps of the absorption line strengths of the 48 objects, ordered by increasing NGC number. For each galaxy, we show the total intensity reconstructed from the full wavelength range of the SAURON spectra (see also Paper III), and the two-dimensional line strength distributions of $\text{Mg } b$, Fe5015 , Fe5270_s and $\text{H}\beta$ overplotted with isophotes of the reconstructed image spaced by single magnitude steps. The maps are all plotted with the same spatial scale, and oriented with respect to the SAURON field for presentation purposes. The relative directions of north and east are indicated by the orientation arrow next to the galaxy title (we note that the orientation and binning of the maps are identical to Papers III and V). The maximum and minimum of the plotting range are given in the tab attached to each parameter map, and the colour bar indicates the colour table used. In order to allow for an easy comparison between galaxies, the plotting range of the $\text{H}\beta$ maps is fixed to 1.0–2.9 Å (with the exception of NGC 3032, 3156, 4150 which show larger $\text{H}\beta$ absorption strengths in the central parts). The colours are adjusted such that blue to green shades correspond to the $\text{H}\beta$ strength predicted for old stellar populations (~ 12 Gyr), while stronger $\text{H}\beta$, corresponding to the presence of younger stellar populations, are represented by red and yellow shades (see e.g. Thomas et al. 2003). For the metal line maps, we use an independent plotting range for each galaxy in order to better visualize the line strength gradients across the maps.

For some galaxies, we found non-physically large values of the Fe5015 line strength in the outer regions where many individual lenslets are averaged to achieve the target S/N of 60. The same effect can be seen to a much lesser extent in $\text{Mg } b$ maps. Similar to the continuum variations which cause some of the $\text{H}\beta$ measurements to be corrupted in the outskirts, we suspect that the $\text{Mg } b$ and Fe5015 indices are also affected (see Section 3.1.2). Due to the degeneracy between abundance ratio variations and continuum effects, we cannot apply a continuum correction for the metal lines. Therefore, we decided to remove the most affected bins by hand from the final data cubes. These bins are indicated with grey colour in the line strength maps presented in Figs 10(a)–(l).

5.1 Overview of the line strength maps

The maps in Figs 10(a)–(l) show a wealth of structures, and we give comments on individual galaxies in Appendix A. Some general trends are apparent, and we discuss these briefly in the following. A full stellar population analysis of the line strength maps with the help of stellar population models will be presented in a future paper in this series.

The metal line strength maps often show negative gradients with increasing radius roughly consistent with the morphology of the light profiles. Remarkable deviations from this trend exist: NGC 3032, 3156, 4150 and 4382 show a central depression in $\text{Mg } b$ line strength. This structure is always accompanied by a strong peak in the $\text{H}\beta$ maps indicating the presence of a recent post-starburst or even low-level ongoing star formation. Interestingly, the Fe maps of post-starburst galaxies do not always show a depression such as the $\text{Mg } b$ index which can be understood in the reduced sensitivity to stellar population age of Fe indices.

Significant, but low-level, deviations between isoindex contours of the metal indices and the isophotes are discussed separately in Section 5.2. We find that enhanced $\text{Mg } b$ absorption strength is connected to fast-rotating components (as defined in Cappellari et al.

2006, hereafter Paper IV) in the galaxies. Perhaps the strongest case in our sample is presented in the $\text{Mg } b$ map of NGC 4570 where the $\text{Mg } b$ strength along the major axis runs through a dip outside the bulge region and then begins to rise towards larger radii where the galaxy kinematics start to be dominated by an outer disc [see also Fisher, Franx & Illingworth (1996) for a long-slit study of S0s].

For galaxies with weak $\text{H}\beta$ absorption ($\simeq 1.4$ Å), the maps show typically mild positive gradients or are consistent with being flat. A few galaxies (e.g. NGC 3489, 7332 and 7457) show $\text{H}\beta$ maps with an overall elevated $\text{H}\beta$ line strength indicating a spatially extended, recent star formation episode. Other galaxies (NGC 4382, 4459 and 4526) exhibit a more centrally concentrated region of relatively strong $\text{H}\beta$ absorption pointing towards a more localized star formation event.

Regions of strong $\text{H}\beta$ absorption are often associated with dust features and detected in emission (see emission maps and unsharp-masked images in Paper V). The case of NGC 4526 deserves a special note, since here one can see the direct connection between an almost perfect dusty disc seen close to edge on (apparent in the reconstructed image), and the location of strong $\text{H}\beta$ absorption indicating the presence of young (~ 1 Gyr) stars.

5.2 $\text{Mg } b$ isoindex contours versus isophotes

One of the most interesting aspects of integral-field spectroscopy is the capability to identify two-dimensional structures. For the first time, we can use this in connection with line strength indices and compare isoindex contours with the isophotal shape. One might expect the index to follow the light in slowly rotating giant elliptical galaxies, since the stars are dynamically well mixed. However, one could imagine that dynamical substructures with significantly different stellar populations could leave a signature in line strength maps which are sensitive to, for example, metallicity.

The $\text{Mg } b$ index is the best determined index in our survey, and potential differences between isoindex contours and isophotes should be most apparent. Indeed, we find a number of galaxies where the isoindex contours clearly do not follow the isophotes, e.g. NGC 4570 and 4660. Both galaxies show fast-rotating components (see Paper III) along the direction of enhanced $\text{Mg } b$ strength. In order to further study such a possible connection, we determine the best-fitting (χ^2 sense), simple, elliptical model for each of the reconstructed images and $\text{Mg } b$ maps in our survey. For this model, we impose a constant ellipticity and position angle as a function of radius, where the position angle is determined as the average position angle of the reconstructed image. An example of this procedure is shown in Fig. 11. We then compare the derived characteristic ellipticities for the isophotes and $\text{Mg } b$ maps with each other. Clearly, such a simple model does not give a good fit to all galaxies, but it provides us with a robust, global shape measurement of the isoindex contours as compared to the isophotes.

In order to avoid confusion by the presence of significant dust absorption, we exclude the following galaxies from the analysis: NGC 2685, 3032, 3156, 3489, 4374 and 4526. Furthermore, we exclude NGC 4486 because of the presence of the non-thermal emission from the well-known jet. This leaves a sample of 41 galaxies.

The results of the ellipse fitting are shown in Fig. 12. Errors are evaluated via 50 Monte Carlo simulations per map where the $\text{Mg } b$ strength of each bin is varied according to the index errors. Additionally, we allowed for a 5 per cent fraction of the data values

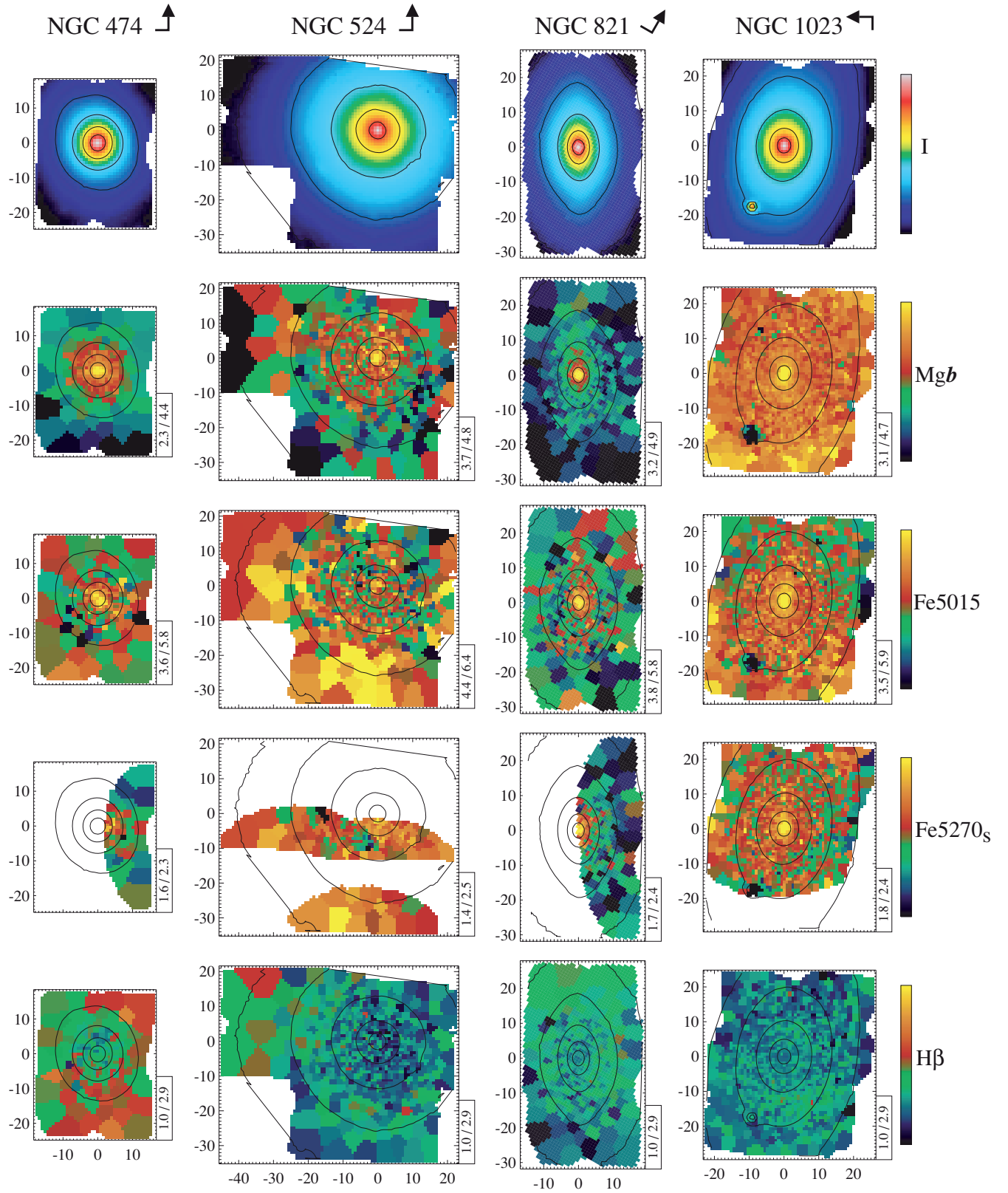


Figure 10. Line strength maps of 48 E and S0 galaxies. (a)–(l) Maps of the line strength 48 E and S0 galaxies in the SAURON representative sample. The SAURON spectra have been spatially binned to a minimum S/N of 60 by means of the centroidal Voronoi tessellation algorithm of Cappellari & Copin (2003). All maps have the same spatial scale. From top to bottom: (i) reconstructed total intensity; (ii) $Mg\,b$ line strength; (iii) $Fe5015$ line strength; (iv) $Fe5270_s$ line strength and (v) $H\beta$ line strength.

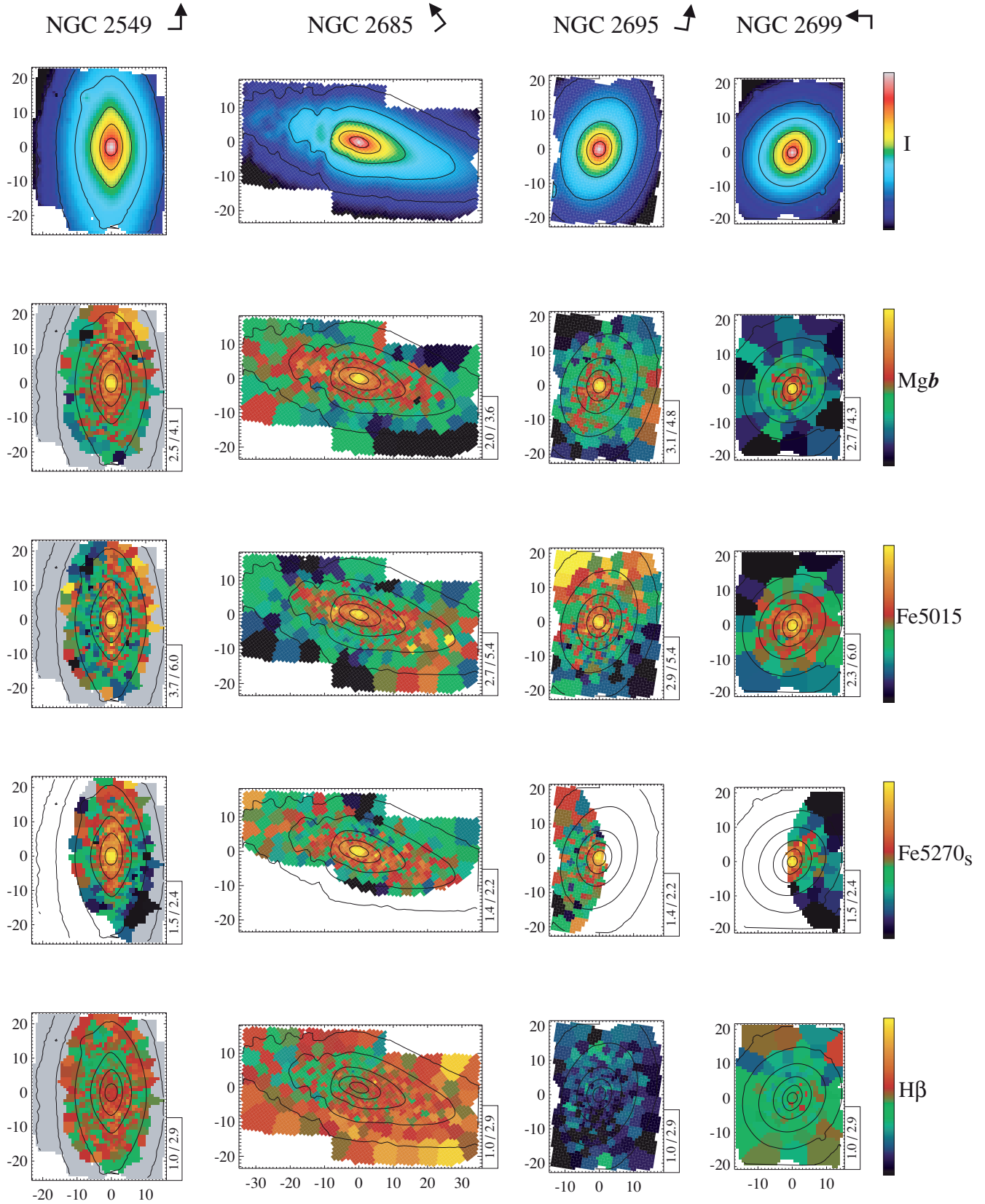


Figure 10 – continued

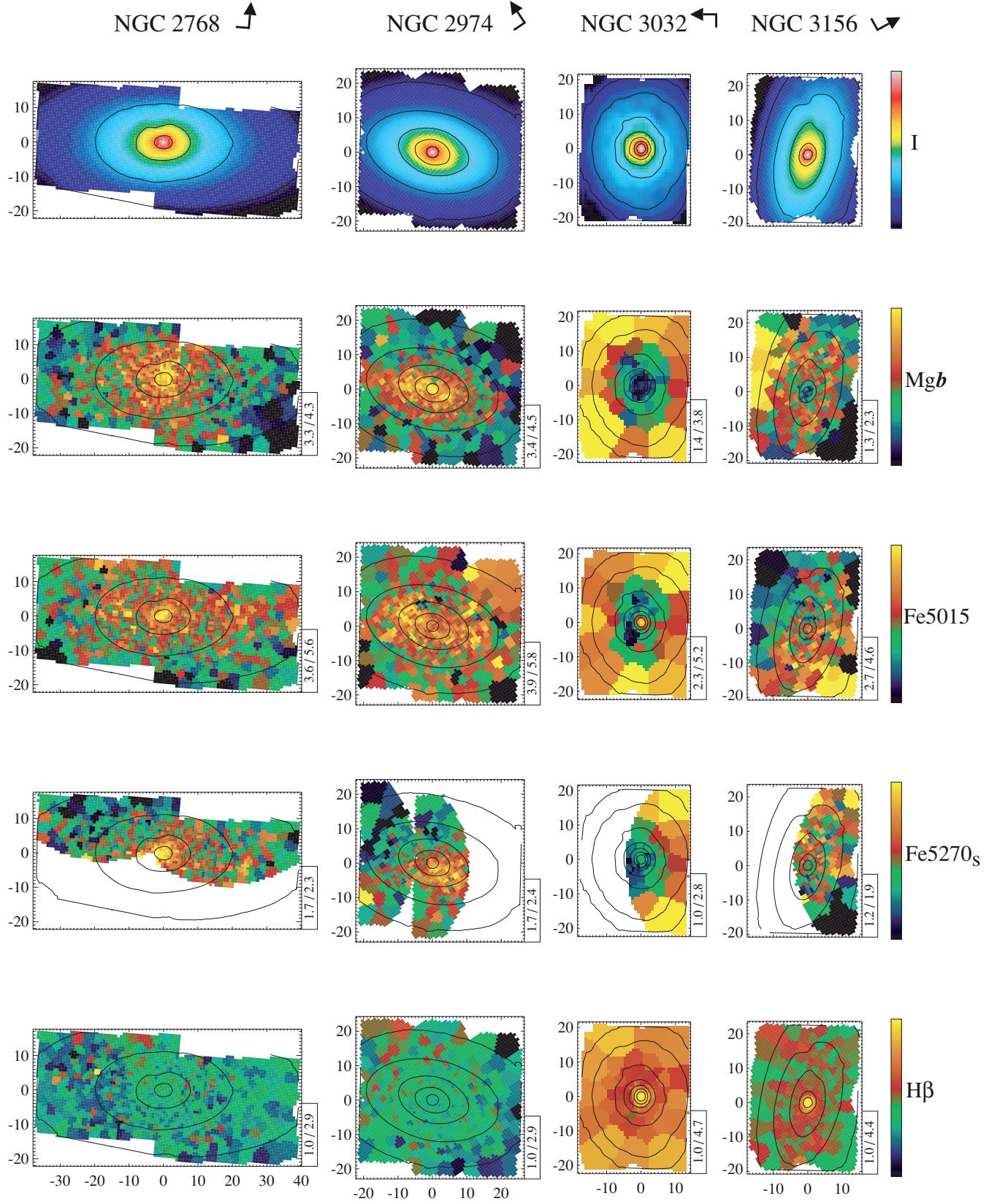
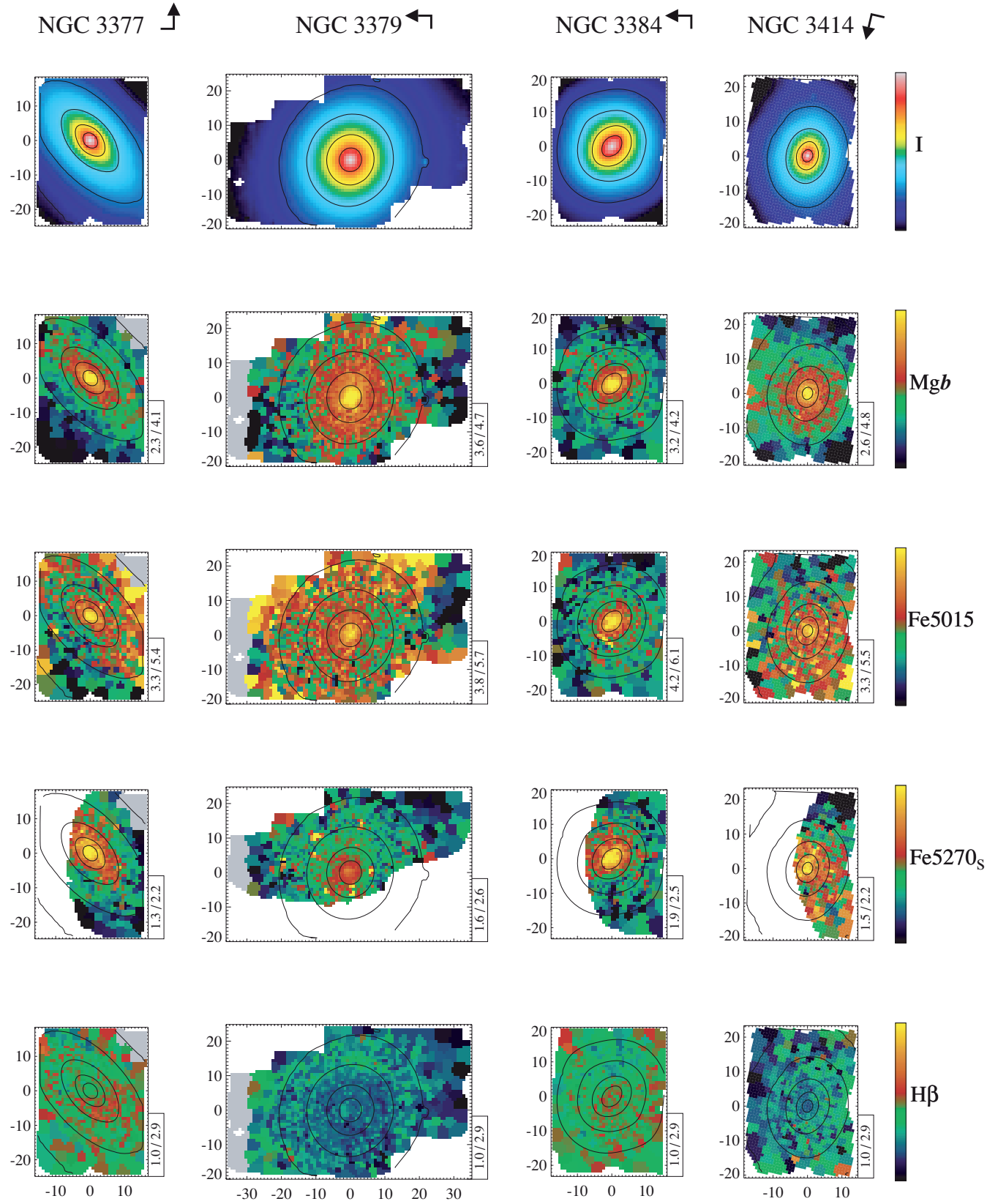


Figure 10 – continued

Figure 10 – *continued*

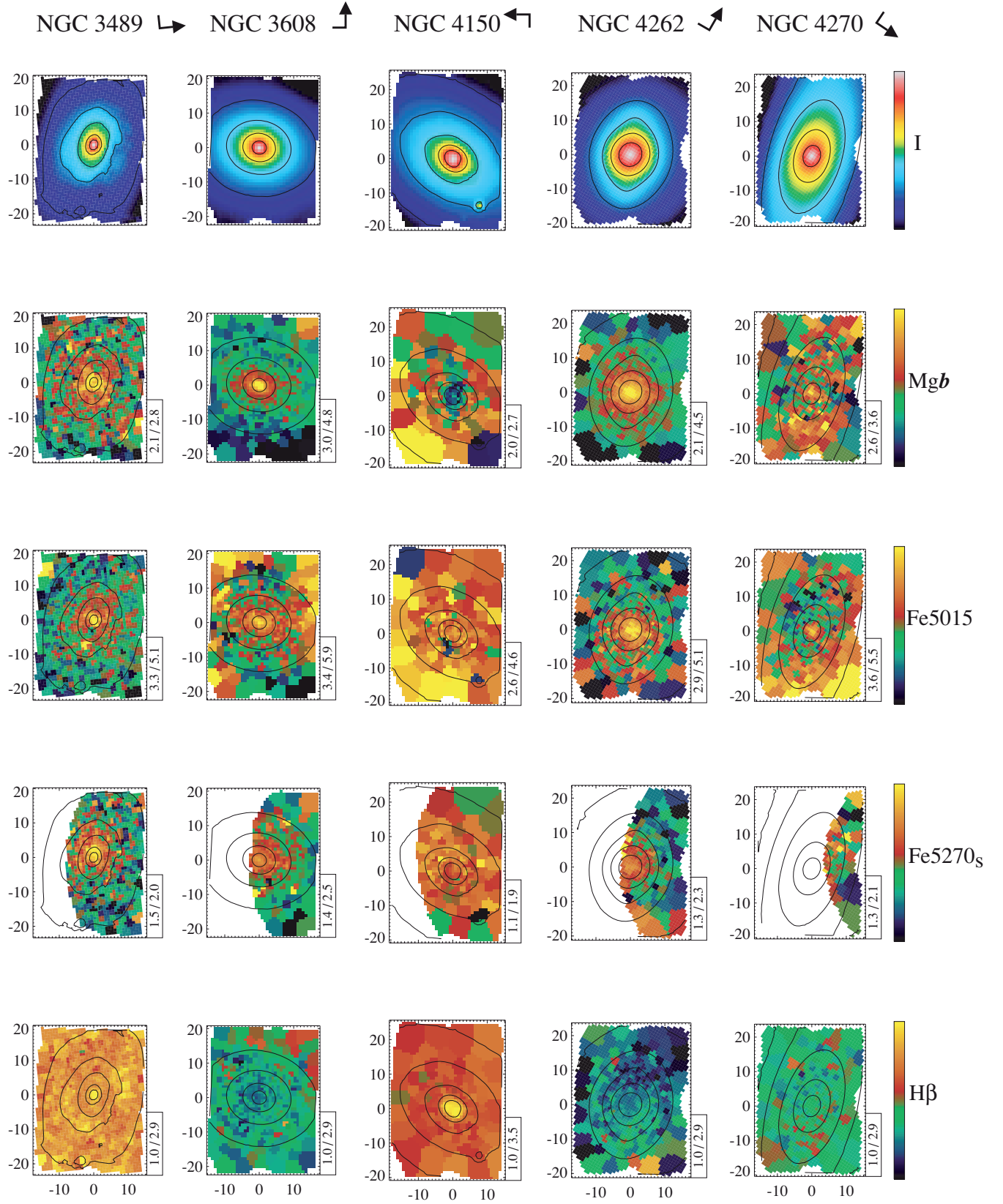


Figure 10 – continued

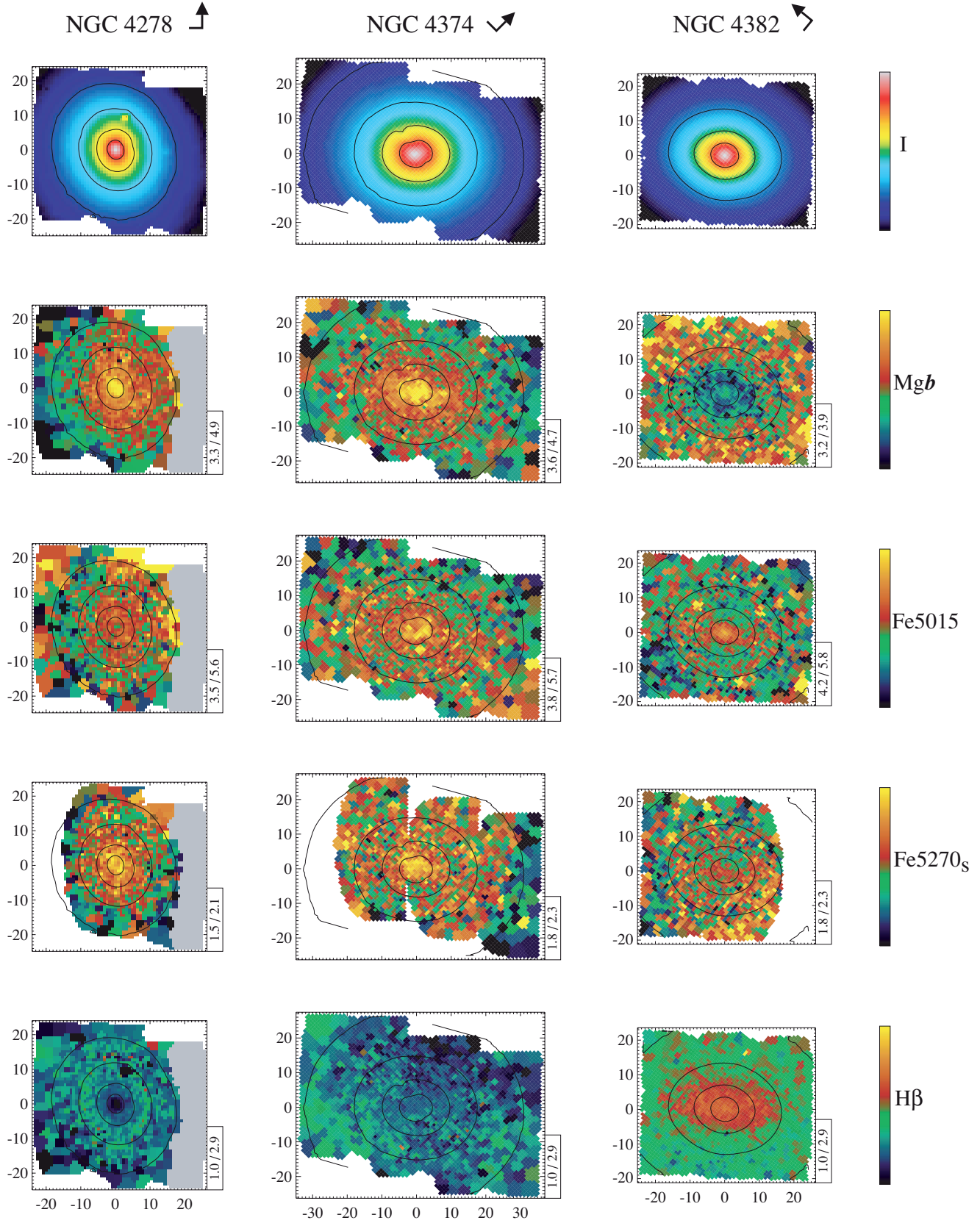


Figure 10 – continued

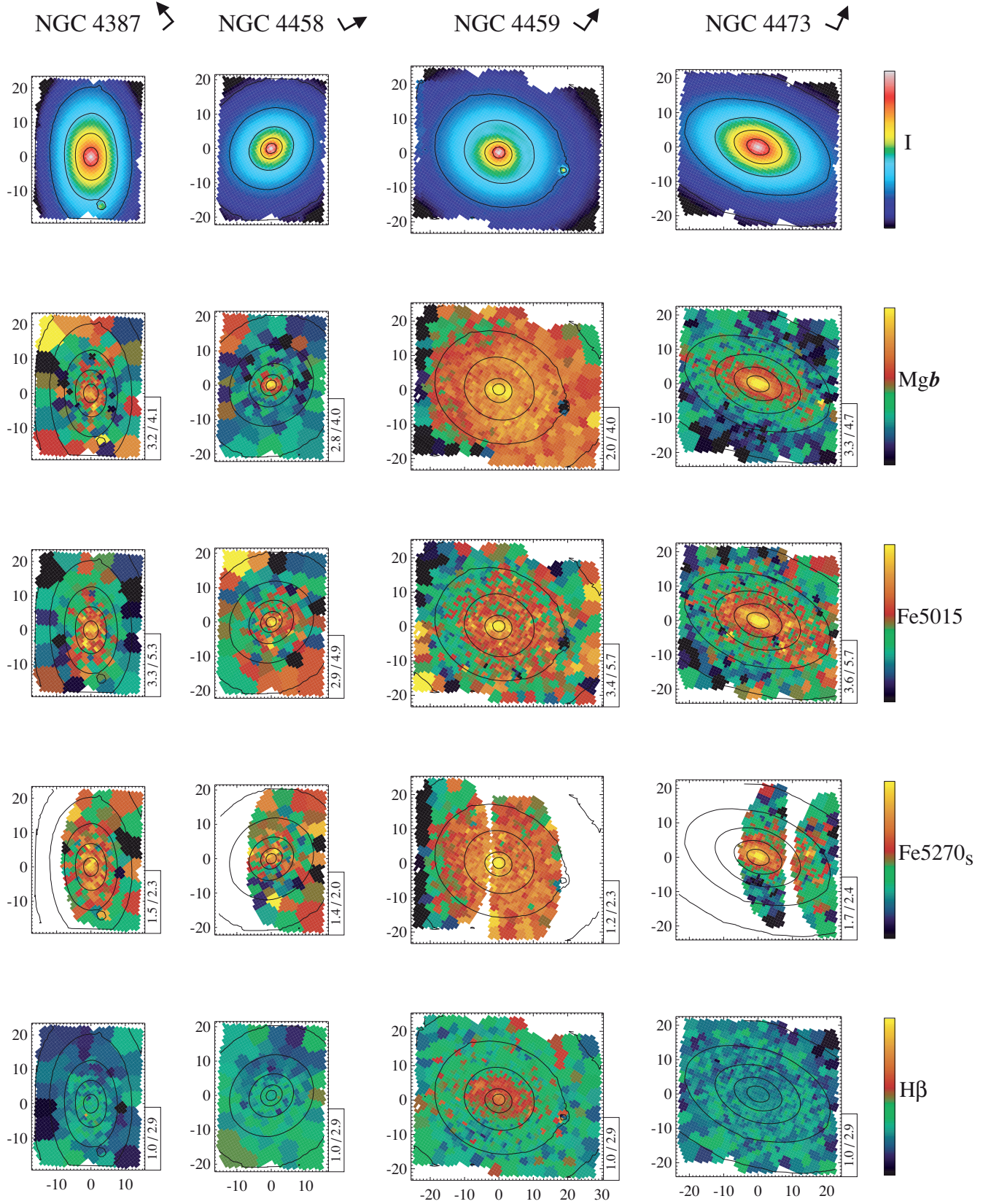
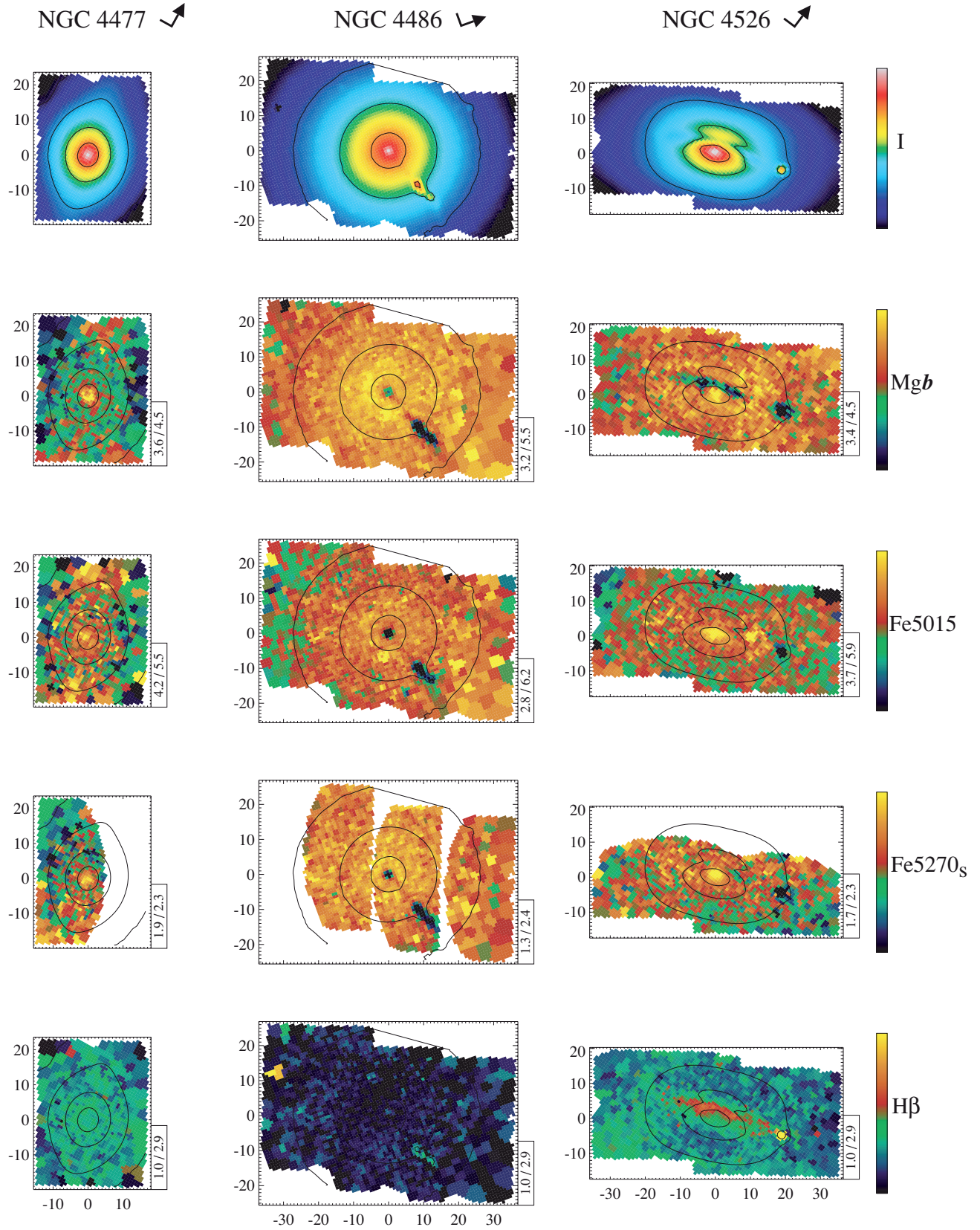


Figure 10 – continued

Figure 10 – *continued*

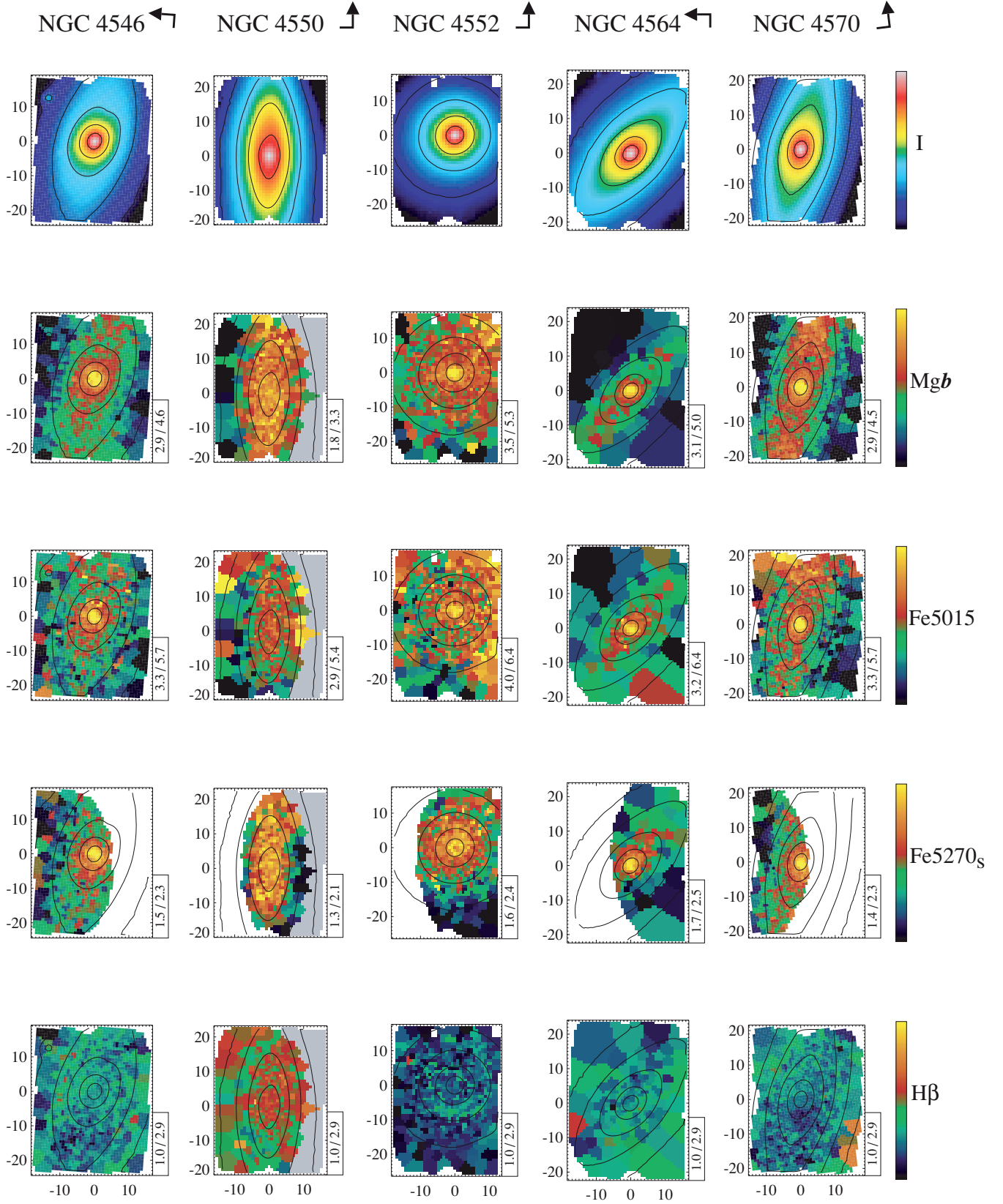
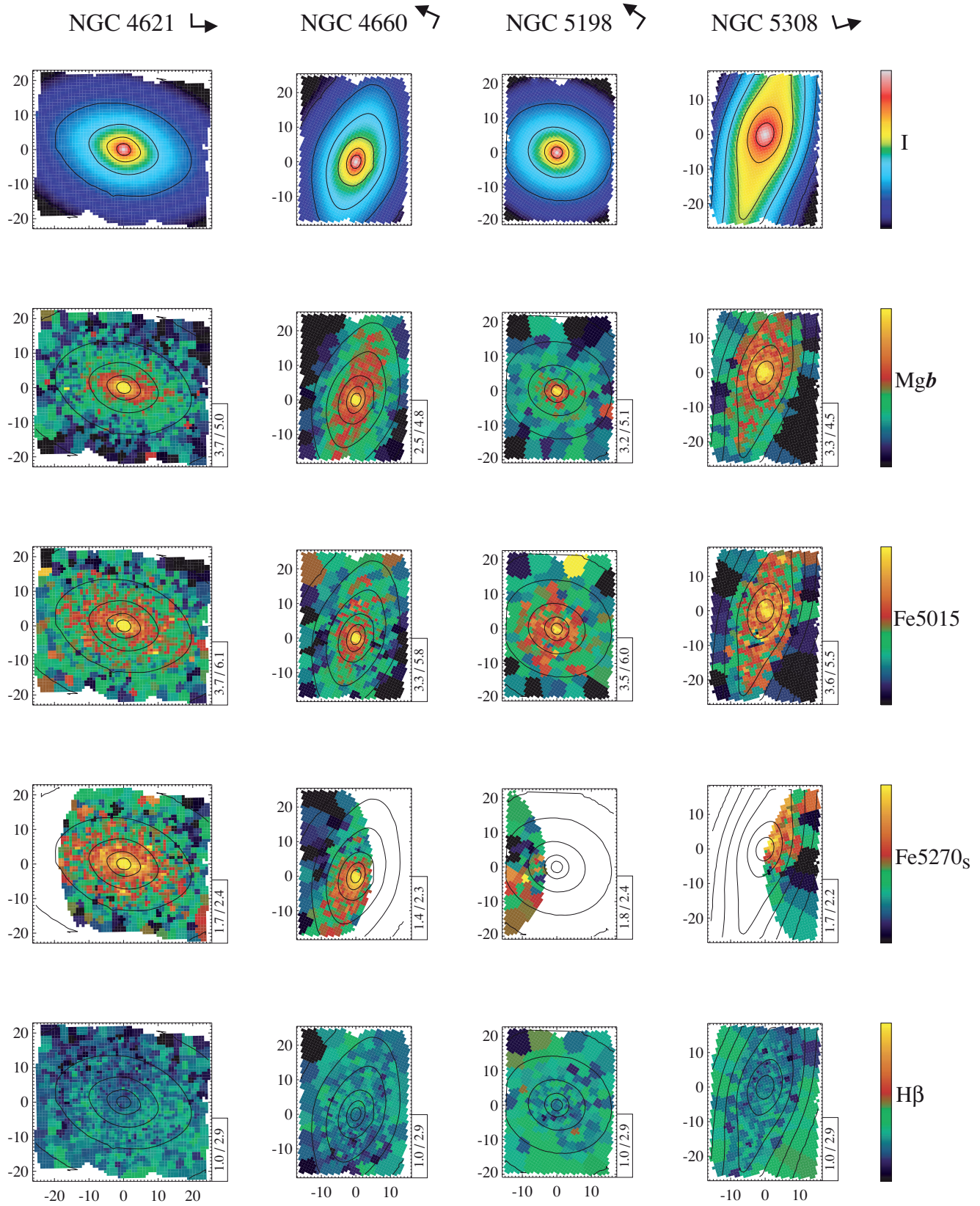


Figure 10 – continued

Figure 10 – *continued*

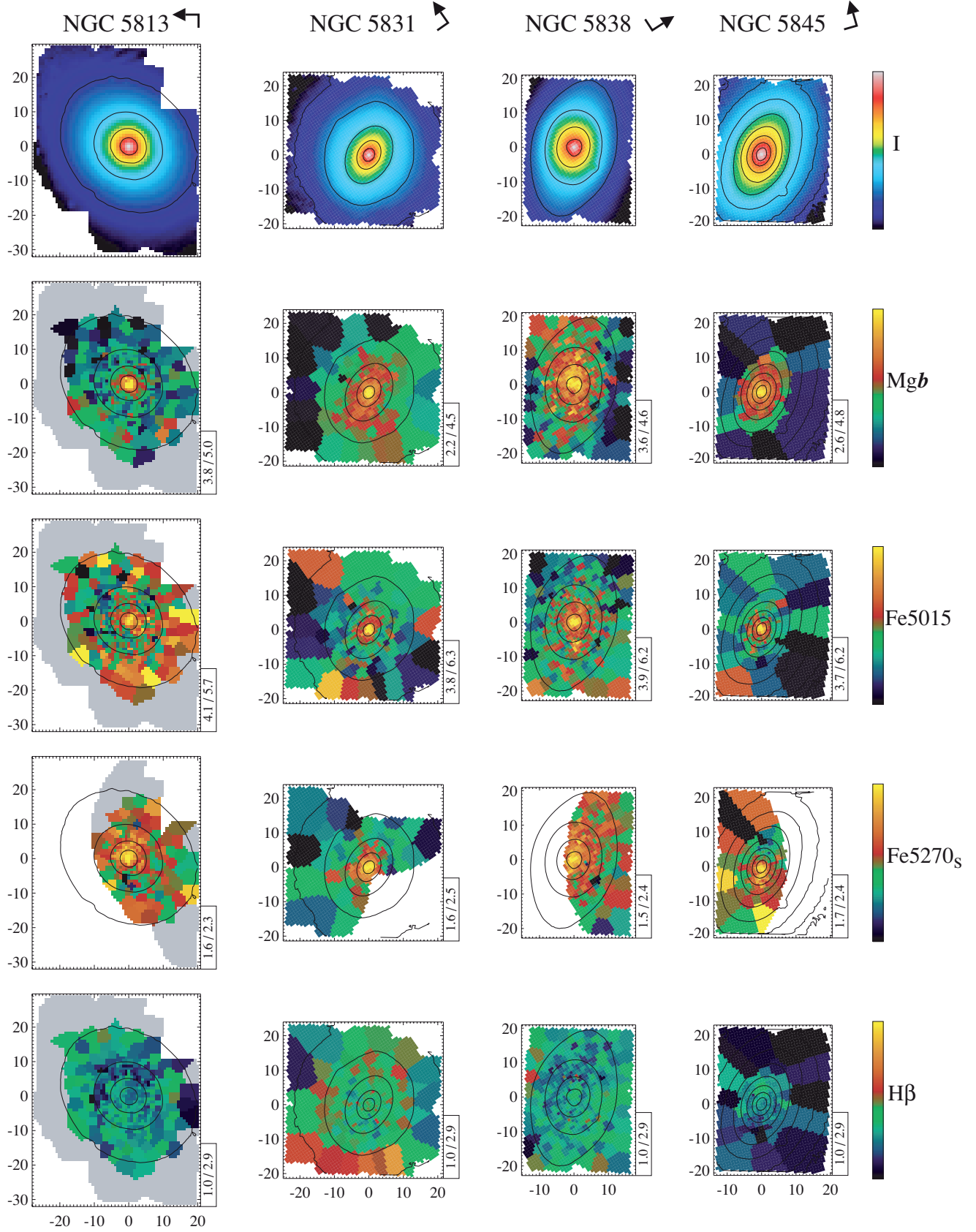
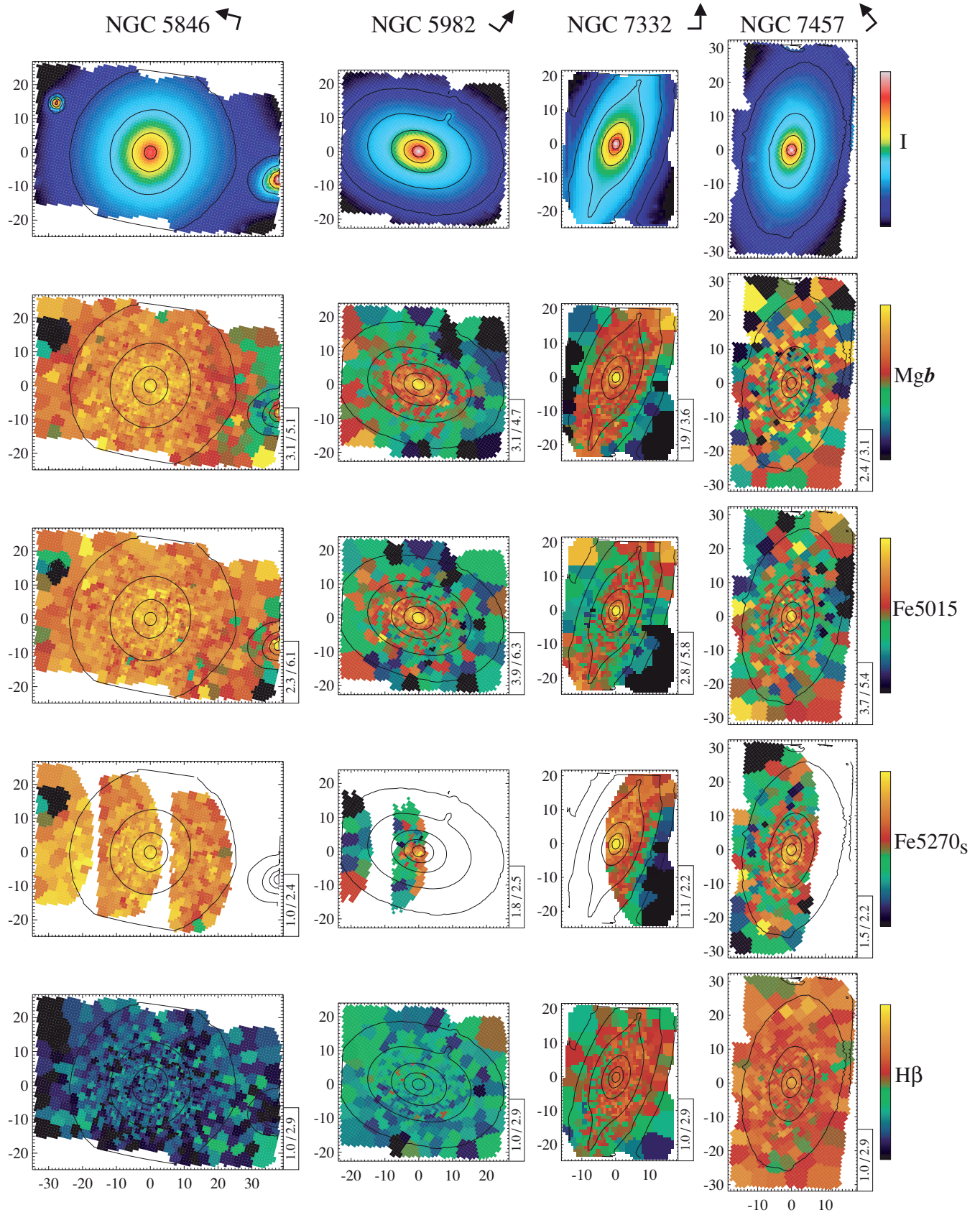


Figure 10 – continued

Figure 10 – *continued*

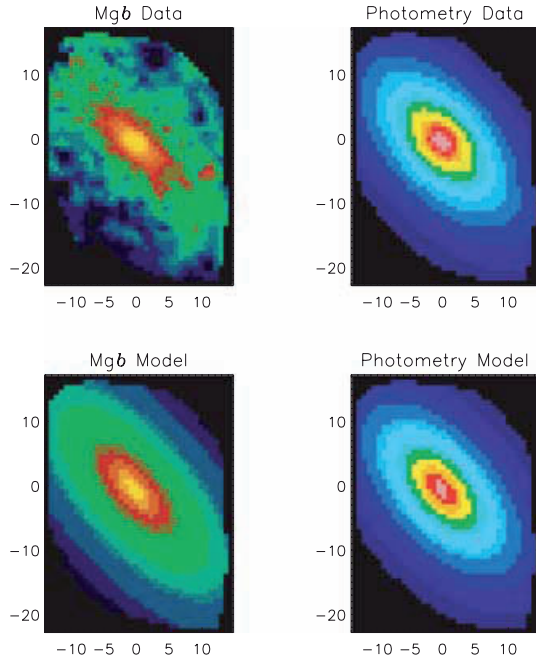


Figure 11. Top row: the interpolated $Mg\,b$ map and the reconstructed image of NGC 3377. Bottom row: the best-fitting elliptical model with constant position angle and ellipticity to the $Mg\,b$ map and the reconstructed image. The best-fitting ellipticity for the isophotes and the $Mg\,b$ map is 0.473 ± 0.003 and 0.573 ± 0.022 , respectively. The x - and y -axis are given in arcsec; north is up and east to the left.

to be considered as outliers and varied those data points by five times its original error. We required a minimum error of $0.08\,\text{\AA}$ per bin⁸ and also excluded all bins covering more than 20 individual lenses from the analysis.

Applying a 2σ error cut, we find 16 out of the 41 galaxies to be consistent with no deviation between isophotes and isoindex contours. Seven galaxies appear to have rounder isoindex contours than the isophotal shape (NGC 2695, 2699, 2768, 3384, 3414, 4262 and 5845). However, 18 galaxies appear to have more flattened $Mg\,b$ contours than the isophotes (NGC 821, 2974, 3377, 3608, 4278, 4382, 4473, 4477, 4546, 4550, 4564, 4570, 4621, 4660, 5831, 5838, 5982 and 7332). Most of these galaxies show a high degree of rotational support and significant h_3 terms. Thus, the flattened $Mg\,b$ distribution suggests that the fast-rotating components in these galaxies exhibit a stellar population different from the main body. The enhanced $Mg\,b$ strength can be interpreted to first order as higher metallicity and/or increased $[\text{Mg}/\text{Fe}]$ ratio. Furthermore, it is evident from the line strength maps that the detailed isoindex shapes cannot always be modelled with a simple elliptical structure. For example, in NGC 4570 one can see a central bulge component with a strong radial $Mg\,b$ gradient, while at larger radii the onset of a disc component with strong $Mg\,b$ is visible (e.g. van den Bosch & Emsellem 1998). A detailed analysis of the line strength distribution and its possible connection to the kinematics will be presented in a forthcoming paper.

⁸In the central, high S/N regions of the $Mg\,b$ maps, our internal error estimates are very small and we use a minimum error of $0.08\,\text{\AA}$ to reflect systematic errors.

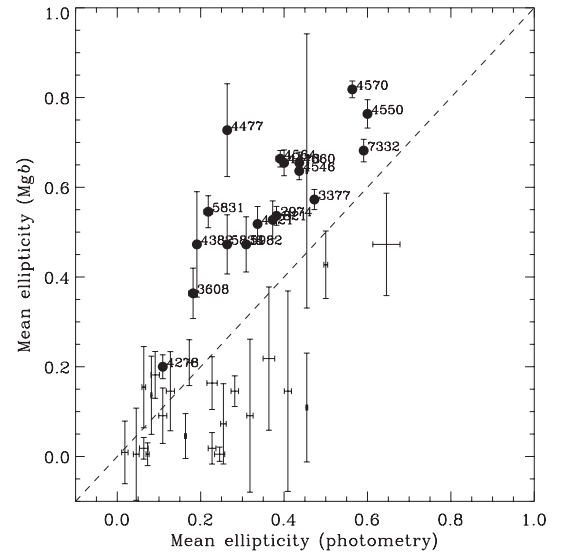


Figure 12. Comparison of the average ellipticity of constant $Mg\,b$ strength with the best-fitting elliptical model of the isophotes. Errors are evaluated by a Monte Carlo simulation and represent 1σ errors. All galaxies which are more than 2σ above the one-to-one line are indicated by filled circles and their galaxy names.

6 LINE STRENGTH GRADIENTS AND APERTURE CORRECTIONS

6.1 Line strength gradients

A number of previous studies have investigated line strength gradients with the help of long-slit data (e.g. Gorgas, Efstathiou & Salamanca 1990; Carollo, Danziger & Buson 1993; Davies et al. 1993; Fisher et al. 1996; Mehlert et al. 2003). Line strength gradients can be used to study the formation history of early-type galaxies since different formation models predict different gradients. In a nutshell, monolithic collapse models (Carlberg 1984) predict steep metallicity gradients with metal-rich centres, whereas hierarchical models, following a merger tree, predict shallower gradients due to the dilution of any line strength gradients existing in the pre-merger units (White 1980).

We now derive line strength gradients from the SAURON sample. First, all indices are expressed in magnitudes (as is the well-known Mg_2 index) which is indicated by a prime sign [$'$]. The conversion between an index measured in \AA and magnitudes is

$$\text{index}' = -2.5 \log \left(1 - \frac{\text{index}}{\Delta\lambda} \right), \quad (3)$$

where $\Delta\lambda$ is the width of the index bandpass.

In Section 5.2, we have mentioned the fact that overall, the morphology of the line strength maps resembles the corresponding photometry. This motivated our choice to derive robust and simple line strength gradients by averaging the indices along lines of constant surface brightness (isophotes) with equal steps in log flux. The average line strength in each radial bin is derived after applying a 3σ clipping algorithm. The radius for each bin is calculated as the median major axis radius normalized to the effective radius along the major axis $a_e = R_e/\sqrt{1-\epsilon}$, where R_e is the effective radius and ϵ is the average ellipticity of the galaxy within the SAURON field. The effective radii R_e (see Table 5) are derived with a $R^{1/4}$ growth curve analysis from our wide-field Michigan–Dartmouth–MIT (MDM, 1.3-m) imaging survey of the E/S0 sample,

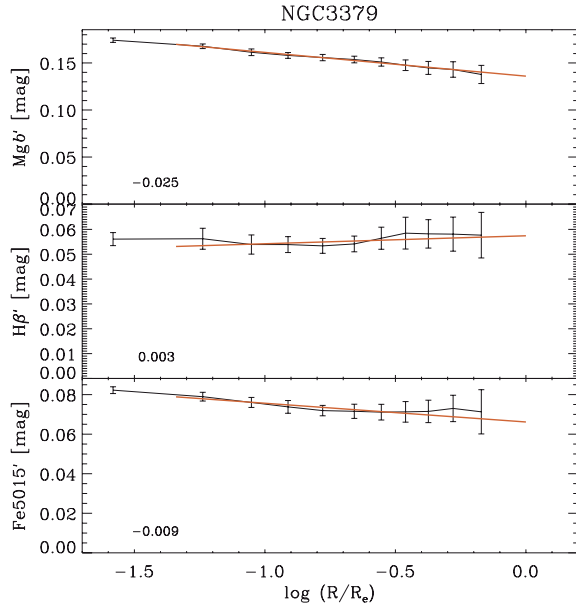


Figure 13. Line strength gradients for NGC 3379 as a function of $\log(R/R_e)$ along the major axis. Error bars reflect the 1σ scatter of data points along a given band of constant surface brightness. The red line represents the best-fitting straight line to the data. The radial extent of the red line reflects the fitting range in $\log R/R_e$. The fitted line strength gradients are noted in the lower left of each panel.

supplemented by archival *Hubble Space Telescope* (HST) images. The photometry and analysis thereof will be presented in a forthcoming paper of this series.

For each galaxy, we fit an error-weighted straight line to the index values at a given radius such that gradients are defined as

$$\Delta \text{index}' = \frac{\delta \text{index}'}{\delta \log(R/R_e)}. \quad (4)$$

The error of the index value in each surface brightness bin is taken as the 1σ scatter of the data points within this bin after applying a 3σ clipping algorithm. We further restrict the fitting range to radii between 2 arcsec and R_e . An example fit to the data of NGC 3379 is shown in Fig. 13.

In Fig. 14, we present for the full sample the fitted gradients for the $H\beta$, Fe5015, and $Mg\,b$ indices plotted against the average (luminosity-weighted) index values within a circular aperture of one-eighth of an effective radius ($R_e/8$; see Section 7 for details). For elliptical galaxies, the $H\beta$ gradients have a mean value of 0.000 ± 0.006 , i.e. they are consistent with a flat relation (see also Mehlert et al. 2003). The lenticular galaxies show a range in $H\beta$ gradients where stronger (negative) gradients are correlated with increasing central ($R_e/8$) $H\beta$ absorption strengths. This is mostly a consequence of the presence of galaxies in our sample which harbour young stars in the central regions, but have little or no star formation in the outer parts. If these young stars amount only to a small fraction in mass, the gradients will within a few Gyr become shallower and the central $H\beta$ absorption strength will decrease, moving the galaxies back to the bulk of points in Fig. 14.

We find mostly negative gradients for the metal line gradients, consistent with the literature (e.g. Carollo et al. 1993; Davies et al. 1993; Kobayashi & Arimoto 1999). Median gradients for Fe5015' and $Mg\,b'$ are -0.014 and -0.025 , respectively. Using the full sample, we find significant correlations between the line strength gradients and the average values within ($R_e/8$) for Fe5015 and $Mg\,b$.

The correlation coefficient derived from a (non-parametric) Spearman rank-order test is -0.55 (<1 per cent) and -0.49 (<1 per cent), for the Fe5015' and $Mg\,b'$ indices, respectively. The probability that the parameters are not correlated is given in parentheses.

A possible correlation between the Mg gradient (as measured by the Mg_2 index) and the central Mg line strength had been suggested by (Gonzalez & Gorgas 1995, see also Carollo et al. 1993), but some other investigations failed to detect a significant correlation (e.g. Kobayashi & Arimoto 1999; Mehlert et al. 2003). New long-slit observations of a sample of 82 early-type galaxies presented by Sánchez-Blázquez (2004) do confirm the trend found by Gonzalez & Gorgas (1995).

In our sample, the correlation for the $Mg\,b'$ index is largely driven by the (lenticular) galaxies with $Mg\,b' < 0.13$. These galaxies are the ones with young stars in the central regions. This can be seen in Fig. 15(b) where we show the relation between $H\beta'$ and $Mg\,b'$ gradients. There is also a good correlation between the gradients of the $Mg\,b'$ and Fe5015' indices as shown in Fig. 15(a) (see also Fisher et al. 1996). This indicates that both indices are sensitive to similar stellar population parameters (e.g. metallicity).

In summary, it appears that in our sample there are significant correlations of the line strength gradients with the central line strength in early-type galaxies. The relations are predominantly driven by the lenticular galaxies and, furthermore, by the presence of young stellar population in the central regions of galaxies. Environmental differences do not seem to play a major role. It is now interesting to explore if the above correlations also hold if line strength gradients are compared to index strength at larger radii, i.e. more representative regions for the galaxies as a whole.

In Fig. 14 (right-hand side panels), we plot the fitted gradients for the $H\beta$, Fe5015, and $Mg\,b$ indices against the index value at $1/4$ effective radius along the major axis. The index value at $1/4$ effective radius is taken to be the value predicted by the fit. We have chosen this particular reference point, since it is within the range of the observed line strength gradients for all galaxies and is more representative of the galaxy as a whole rather than being biased to the central regions.

In this new diagram, we do not find a significant correlation for the Fe5015' index. For the $H\beta$ index, there is still a correlation visible, but it is exclusively driven by the three galaxies in the lower right part of the plot. The situation for $Mg\,b'$ appears more complex. There is no significant correlation for the full sample, while the S0s show a trend similar to the one derived for the $1/8$ effective radius values. The elliptical galaxies even appear to follow a *positive* correlation between line strength gradient and $Mg\,b'$ strength at $R_e/4$. However, the latter trend is not significant.

We conclude that for early-type galaxies in our sample there is a correlation between line strength gradients of $H\beta$, Fe5015 & $Mg\,b$ and centrally averaged line strength values ($R_e/8$). These correlations are driven to a large extent by the presence of young stellar populations in the central regions of (typically lenticular) early-type galaxies, and are thus caused by galaxies which have recently experienced secondary star formation which may account only for a minor fraction of the total galaxy mass.

6.2 Aperture corrections

For studies of galaxies over a significant redshift and size range, aperture corrections have to be applied in order to allow for a fair comparison of kinematic and stellar population parameters (e.g. Jørgensen, Franx & Kjaergaard 1995). In Paper IV, we present an aperture correction for the luminosity-weighted second moment

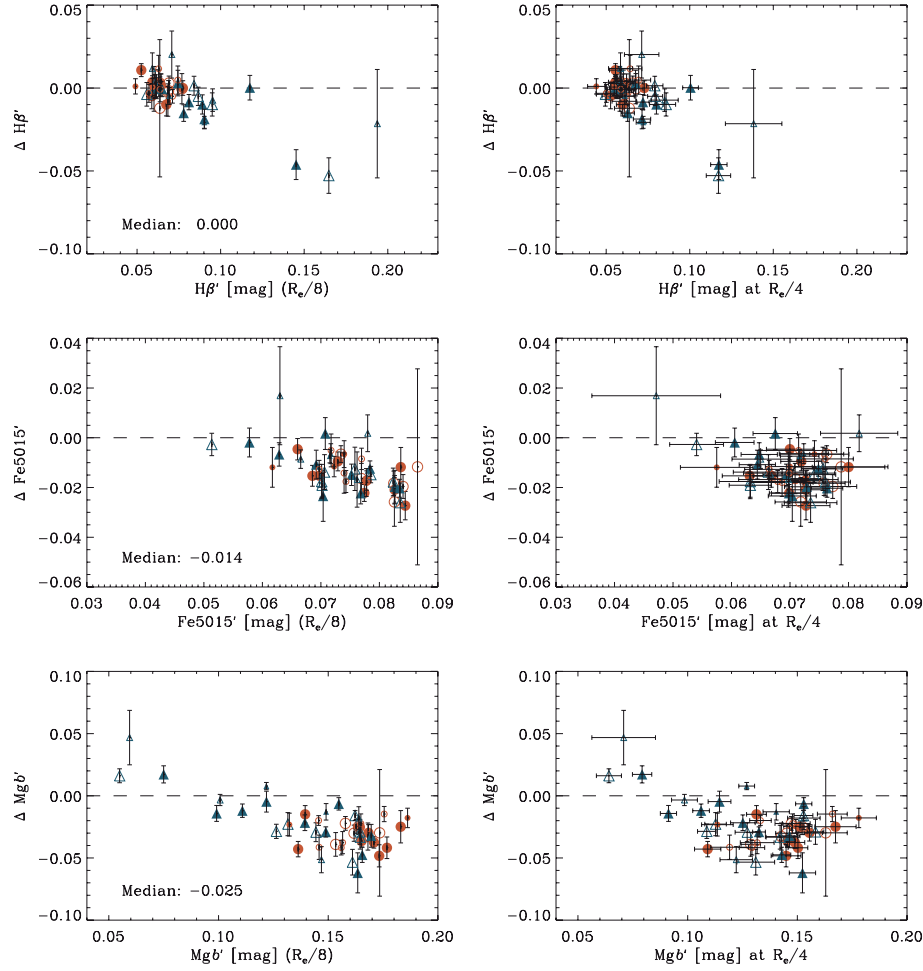


Figure 14. Left-hand column of panels: index gradients as a function of luminosity-weighted index values within a circular aperture of one-eighth of an effective radius ($R_e/8$). The red filled and open circles are cluster and field ellipticals, respectively; blue filled and open triangles are cluster and field S0s, respectively. The smaller symbols indicate galaxies for which our data cover less than half the effective radius. Error bars are formal errors from the straight line fits. A gradient of 0.0, i.e. a flat relation, is indicated by the dashed lines. Median gradients are given in the lower left of each panel (see text for details). Right-hand column of panels: index gradients as a function of (fitted) line strength at 1/4 effective radius along the major axis. Symbols are the same in both diagrams.

of the LOSVD (σ), while here we present aperture corrections for the line strength indices $H\beta$, Fe5015 and $Mg\,b$.

For this, we show in Fig. 16 the luminosity-weighted line strength measurements within an aperture of radius R , normalized to their value at half of the effective radius. The profiles were measured by co-adding the SAURON spectra within circular apertures of increasing radius for all 39 early-type galaxies which have data out to at least half of the effective radius. If the SAURON FoV does not cover the complete circular aperture at a given radius, we calculate an equivalent radius of a circular aperture which matches the area of the SAURON FoV.

The metal line indices show generally a decreasing profile with increasing (R/R_e), while the $H\beta$ index shows a wide range in aperture corrections. Typical aperture corrections are small where a correction from 1/4 effective radius to 1 effective radius would amount to approximately 0.5 per cent for the $H\beta$ index and ~ 9 per cent for the metal indices. However, it is clear that substantial galaxy-to-galaxy variations in the profiles exist. Particularly, for galaxies harbouring a young stellar population in the centre (i.e. positive $Mg\,b$ gradients) the application of an average aperture correction can be severely wrong.

The best-fitting power-law relations to the line strength measurements as a function of normalized radius ($\frac{R}{0.5R_e}$) were determined for each galaxy individually by fitting all available data outside $R = 2$ arcsec. Then, a median power-law index and a robustly estimated scatter were derived. These median power-law indices for each absorption feature are only provided as a convenient approximation of the true aperture corrections and are presented in Table 4. They are in reasonable agreement with previously published aperture corrections (Jørgensen et al. 1995; Mehlert et al. 2003).

7 INTEGRATED INDEX- σ RELATIONS

After the presentation of the complete line strength maps (Section 5) and the average gradients (Section 6), we now present luminosity-weighted line strength indices averaged over a circular aperture. We focus on one key diagnostic: the index- σ relations.

Our integrated measurements were derived by averaging the (luminosity-weighted) spectra within a circular aperture with a radius of ($R_e/8$), but imposing a minimum aperture of 2.4×2.4 arcsec² (3×3 pixel²). From this high S/N spectrum, we re-measure the kinematics (V , σ , h_3 and h_4) as described in Paper III (see also

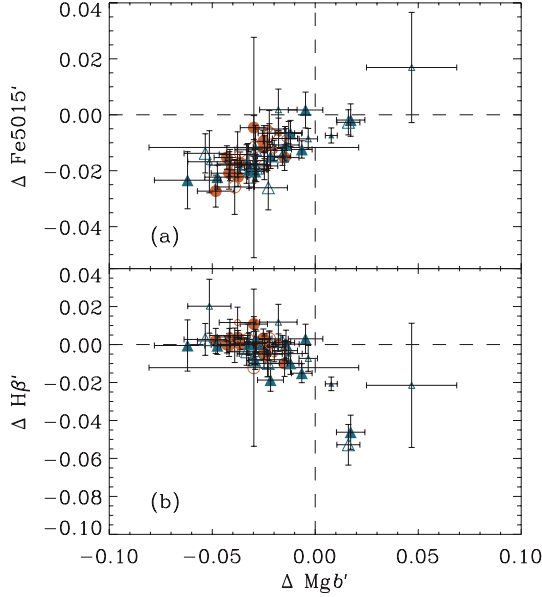


Figure 15. (a) Fe5015' gradients versus Mg b' gradients. (b) Hβ' gradients versus Mg b' gradients. The red filled and open circles are cluster and field ellipticals, respectively; blue filled and open triangles are cluster and field S0s, respectively. The smaller symbols indicate galaxies for which we do not cover half the effective radius. Error bars are formal errors from the straight line fits.

Cappellari & Emsellem 2004) and then determine the line strength as presented in Section 4. Because of limited field coverage, we do not quote central averaged Fe5270_s measurements for 11 galaxies (NGC 474, 524, 821, 2695, 2768, 3608, 4270, 5198, 5308, 5846 and 5982). In a further eight galaxies, the ($R_e/8$) aperture is not fully covered by our maps; however, only a few bins, corresponding to less than 10 per cent coverage, are missing and we judge the average spectrum to be still a good representation of the galaxy.

In order to provide a more global measurement for each galaxy, we also derived a central averaged spectrum from all data available within one effective radius. Because of the sometimes severely limited field coverage of the Fe5270_s index, we do not quote one effective radius averages for it. Furthermore, since our line strength maps of the other indices do not always cover the full area of one effective radius we need to assess the degree of necessary aperture corrections. The galaxies with the smallest coverage (NGC 4486 and 5846) feature line strength data out to about 30 per cent of R_e . Even in these extreme cases, we estimate corrections to be small (<8 per cent; see Section 6.2). For the 32 galaxies for which the data extend to less than one effective radius, we apply the corrections of the form given in Table 4. The median coverage of the line strength maps is $0.8 R_e$. A subset of one R_e index measurements is used in Paper IV to determine stellar mass-to-light ratios (M/L) and compare them with high-fidelity dynamical estimates of the global M/L inside one R_e .

The final, luminosity-weighted line strength measurements within a circular aperture of ($R_e/8$), and within R_e , are given in

Table 4. Aperture corrections for line strength indices.

$(H\beta_R/H\beta_{norm}) = (R/R_{norm})^{+0.001\pm0.029}$
$(Fe5015_R/Fe5015_{norm}) = (R/R_{norm})^{-0.067\pm0.025}$
$(Mgb_R/Mgb_{norm}) = (R/R_{norm})^{-0.061\pm0.028}$

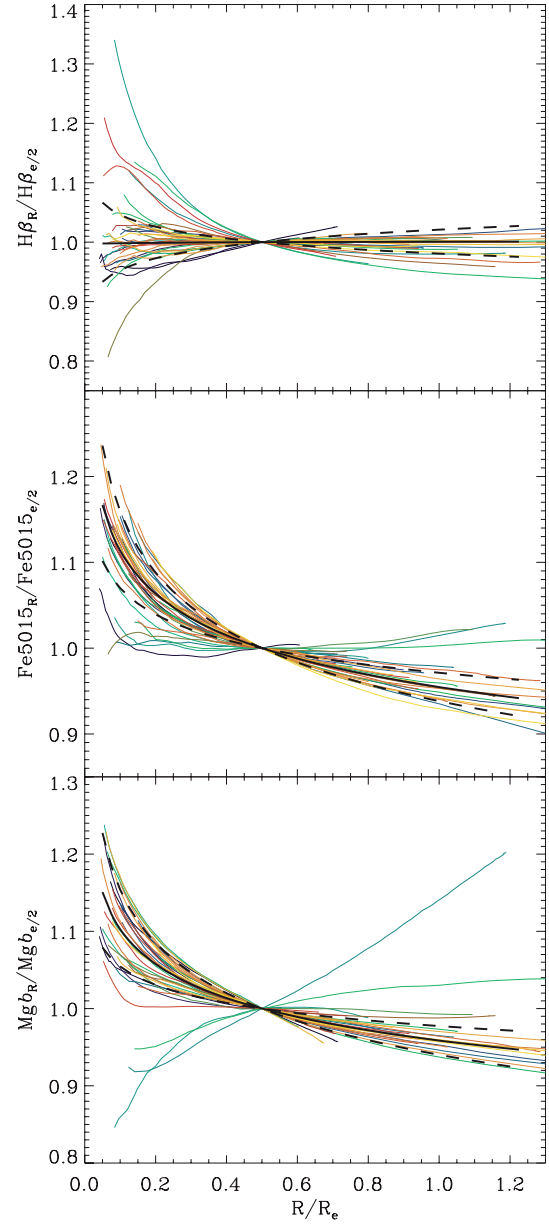


Figure 16. Luminosity-weighted index measurements within an aperture of radius R , normalized to its value at $1/2 R_e$. Each galaxy with data out to at least $1/2 R_e$ is shown with the thin coloured lines. Data points inside $R = 2$ arcsec are excluded to minimize seeing effects. The black line is the median power-law relation $(index_R/index_{norm}) = (R/R_{norm})^p$ where p is given in Table 4. The robustly estimated 1σ errors of the power-law fits are indicated by the dashed black lines (see text for details). The three galaxies with $(Mgb_R/Mgb_{e/2}) < 1.0$ at small radii are NGC 3032, 3156 and 4150.

Table 5. The formal line strength errors are smaller than $\pm 0.01 \text{ \AA}$ for all galaxies. We note, however, that there are systematic errors which we estimate to be of the order of 0.06, 0.15, 0.08 and 0.06 \AA for the Hβ, Fe5015, Mg b and Fe5270_s indices, respectively. For the luminosity-weighted averages of the velocity dispersion, we adopt an error of 5 per cent (see Paper IV).

Our main result for the ($R_e/8$) extractions is shown in Fig. 17. For the index- σ relations, all indices are expressed in magnitudes (see Section 6.1). The Mg b index shows a tight correlation with

Table 5. List of line strength measurements within a circular aperture of $R_e/8$ and R_e .

Name	R_e [arcsec]	R_{\max}/R_e	$\sigma_{e/8}$ [km s ⁻¹] $R_e/8$	H β [Å] $R_e/8$	Fe5015 [Å] $R_e/8$	Mg <i>b</i> [Å] $R_e/8$	Fe5270 _S [Å] $R_e/8$	H β [Å] R_e	Fe5015 [Å] R_e	Mg <i>b</i> [Å] R_e
(1)	(2)	(3)	(4)	(5)	(6)	(7)	(8)	(9)	(10)	(11)
NGC 474	29	0.71	163	1.68	5.45	4.11	–	1.81	4.85	3.45
NGC 524	51	0.61	249	1.39	5.57	4.55	–	1.50	5.38	4.20
NGC 821	39	0.62	202	1.53	5.32	4.35	–	1.57	4.65	3.72
NGC 1023	48	0.56	206	1.49	5.60	4.51	2.34	1.51	4.98	4.19
NGC 2549	20	0.90	142	2.07	5.85	4.05	2.40	2.02	5.10	3.54
NGC 2685	20	1.34	83	2.01	5.05	3.57	2.19	2.04	4.21	3.04
NGC 2695	21	0.95	223	1.31	5.05	4.57	–	1.27	4.34	3.94
NGC 2699	14	1.41	146	1.83	5.86	4.28	2.40	1.76	4.76	3.58
NGC 2768	71	0.39	205	1.70	5.02	4.08	–	1.64	4.43	3.64
NGC 2974	24	1.04	242	1.64	5.27	4.40	2.25	1.71	5.14	4.09
NGC 3032	17	1.19	100	4.57	4.58	1.73	1.62	3.98	4.02	2.14
NGC 3156	25	0.80	61	3.92	3.80	1.60	1.60	3.00	3.66	1.79
NGC 3377	38	0.52	142	1.85	4.95	3.83	2.09	1.86	4.37	3.20
NGC 3379	42	0.64	215	1.43	5.23	4.57	2.20	1.44	4.81	4.15
NGC 3384	27	0.75	158	1.94	5.92	4.16	2.47	1.84	5.12	3.70
NGC 3414	33	0.60	236	1.44	5.08	4.48	2.15	1.50	4.49	3.72
NGC 3489	19	1.05	100	2.82	4.99	2.84	2.01	2.60	4.40	2.60
NGC 3608	41	0.49	189	1.49	5.30	4.36	–	1.60	4.73	3.75
NGC 4150	15	1.39	78	3.47	4.23	2.17	1.69	2.87	4.11	2.35
NGC 4262	10	2.06	199	1.42	5.07	4.54	2.09	1.49	4.46	3.90
NGC 4270	18	1.09	137	1.77	5.09	3.45	–	1.74	4.67	3.24
NGC 4278	32	0.74	248	1.23	4.78	4.67	2.04	1.41	4.59	4.21
NGC 4374	71	0.43	294	1.40	5.19	4.52	2.22	1.42	4.66	4.08
NGC 4382	67	0.38	179	2.16	5.14	3.45	2.12	1.98	4.72	3.36
NGC 4387	17	1.16	96	1.60	5.03	3.92	2.18	1.51	4.42	3.67
NGC 4458	27	0.74	95	1.63	4.49	3.73	1.90	1.59	3.97	3.27
NGC 4459	38	0.71	180	2.16	5.39	3.91	2.27	1.85	4.68	3.43
NGC 4473	27	0.92	198	1.49	5.55	4.59	2.33	1.50	4.88	4.03
NGC 4477	47	0.43	168	1.65	5.15	4.17	2.21	1.59	4.71	3.84
NGC 4486	105	0.29	317	1.14	5.30	5.12	2.22	1.15	4.70	4.62
NGC 4526	40	0.66	240	1.86	5.59	4.32	2.29	1.62	4.93	4.16
NGC 4546	22	0.94	223	1.54	5.49	4.59	2.27	1.54	4.64	3.92
NGC 4550	14	1.28	81	2.14	4.57	3.15	2.00	1.99	4.32	2.93
NGC 4552	32	0.63	277	1.39	5.93	5.04	2.31	1.37	5.33	4.55
NGC 4564	21	1.02	173	1.52	5.98	4.79	2.42	1.55	4.85	4.00
NGC 4570	14	1.43	199	1.45	5.87	4.70	2.34	1.45	4.79	3.99
NGC 4621	46	0.56	229	1.40	5.53	4.73	2.28	1.43	4.75	4.14
NGC 4660	11	1.83	229	1.43	5.87	4.88	2.34	1.47	4.80	4.07
NGC 5198	25	0.80	209	1.49	5.50	4.66	–	1.56	4.70	3.93
NGC 5308	10	2.04	252	1.46	5.42	4.57	–	1.46	4.92	4.23
NGC 5813	52	0.39	231	1.51	5.16	4.58	2.15	1.52	4.74	4.12
NGC 5831	35	0.67	166	1.77	5.55	4.09	2.35	1.78	4.78	3.32
NGC 5838	23	0.87	290	1.64	5.86	4.55	2.35	1.58	5.05	4.19
NGC 5845	5	4.45	285	1.51	6.12	4.80	2.38	1.52	5.38	4.41
NGC 5846	81	0.29	237	1.34	5.50	4.85	–	1.32	4.89	4.38
NGC 5982	27	0.94	269	1.63	5.96	4.50	–	1.60	5.18	3.98
NGC 7332	11	1.91	135	2.28	5.93	3.71	2.30	2.16	4.80	3.17
NGC 7457	65	0.39	62	2.28	4.81	2.88	2.02	2.25	4.33	2.68

Notes. (1) NGC number. (2) Effective (half-light) radius R_e measured from *HST*/WFPC2 + MDM images. (3) Ratio between the maximum radius R_{\max} sampled by the SAURON observations and R_e . The maximum radius is calculated as the equivalent circular radius matching the area of the full SAURON FoV. Note that for five galaxies the values given here are slightly smaller than the ones given in Paper IV since we have removed bad bins for the line strength indices (see also Section 5). (4) Velocity dispersion of the luminosity-weighted spectrum within a circular aperture of $R_e/8$. (5)–(8) Fully corrected line strength index measurements of the luminosity-weighted spectrum within $R_e/8$ for the H β , Fe5015, Mg *b* and Fe5270_S indices. Due to limited field coverage, we cannot determine the Fe5270_S indices for 11 galaxies. (9)–(11) Fully corrected line strength index measurements of the luminosity-weighted spectrum within R_e for the H β , Fe5015 and Mg *b* indices. For galaxies with less than one R_e coverage, we applied the aperture corrections given in Table 4. Formal errors of the line strength indices are below 0.1 Å. We note, however, that there are systematic errors which we estimate to be of the order of 0.06, 0.15, 0.08, 0.06 Å for the H β , Fe5015, Mg *b* and Fe5270_S indices, respectively. For the velocity dispersion, we adopt an error of 5 per cent.

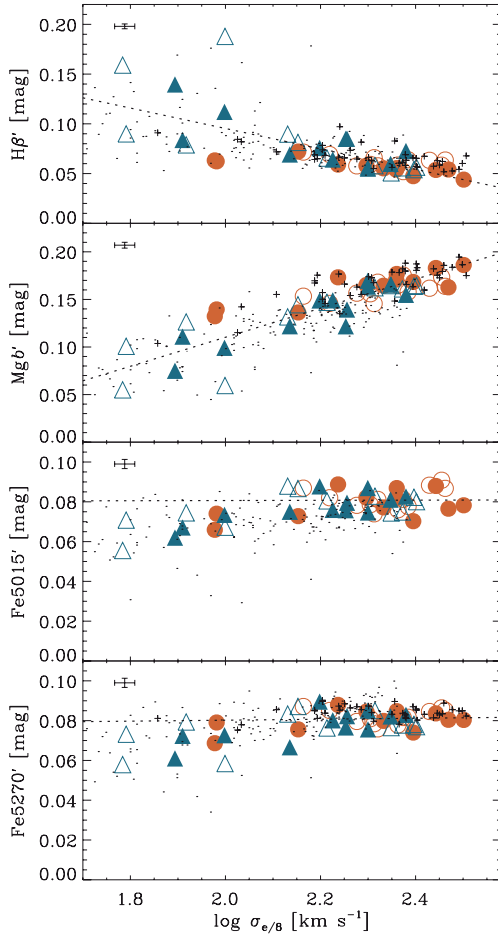


Figure 17. $(R_e/8)$ aperture line strength index versus σ relations. All indices are given in magnitudes. The $\text{Fe}5270_S$ index was converted to the $\text{Fe}5270$ index by using equation (1). The filled and open circles are cluster and field ellipticals, respectively; filled and open triangles are cluster and field S0s, respectively. Mean error bars reflecting mostly systematic errors are shown in the upper left corner of each panel. Small dots are taken from Caldwell et al. (2003). The small plus signs represent the data of González (1993). Data from the literature with $\sigma < 50 \text{ km s}^{-1}$ are not shown. The dashed lines are fits to the data for all galaxies with $\log \sigma \geq 2.1$. The results of the linear fits are summarized in Table 6.

$\log \sigma$ which has been observed by many authors (e.g. Terlevich et al. 1981; Burstein et al. 1988; Bender, Burstein & Faber 1993; Colless et al. 1999; Bernardi et al. 2003; Worthey & Collobert 2003; Denicoló et al. 2005). The $\text{H}\beta$ index shows a relatively tight, negative correlation for galaxies with velocity dispersions $\log \sigma \geq 2.1$. For lower velocity dispersions, there is evidence for an increased scatter (see also e.g. Kuntschner 2000; Caldwell, Rose & Concannon 2003). The deviations from the main relation for galaxies with $\log \sigma < 2.1$ clearly anticorrelate in the $\text{Mg } b$, $\text{H}\beta$ – σ relations.

The two Fe indices show roughly constant index values for velocity dispersions $\log \sigma \geq 2.1$. Similar to the $\text{Mg } b$ and $\text{H}\beta$ – σ relations, we also find an anticorrelation with respect to the fitted relation between Fe and $\text{H}\beta$ index strength at a given σ albeit at lower significance. At lower velocity dispersions, we find there is weak evidence for an increasing index strength with increasing velocity dispersion. Similar trends have been noted by Proctor & Sansom (2002) in an analysis of spiral bulges and E/S0s. The absence of a clear correla-

Table 6. Linear fits to index– σ relations (for $\log \sigma \geq 2.1$).

$\text{H}\beta'$	$= -0.103(\pm 0.017) \log \sigma + 0.301(\pm 0.039)$
$\text{Mg } b'$	$= +0.153(\pm 0.021) \log \sigma - 0.195(\pm 0.050)$
$\text{Fe}5015'$	$= +0.000(\pm 0.010) \log \sigma + 0.080(\pm 0.024)$
$\text{Fe}5270'$	$= +0.002(\pm 0.010) \log \sigma + 0.075(\pm 0.024)$

Notes. The linear fitting was performed by taking into account errors in both variables. The error in the intercepts and slopes has been derived by scaling the errors in the observables by a constant factor until the χ^2 probability is ≥ 0.5 .

tion between Fe indices and the central velocity dispersion has been noted by several authors (e.g. Fisher et al. 1996; Jørgensen 1999), and we can confirm this for our sample. However, for other samples a significant correlation between Fe indices and the central velocity dispersion has been found (e.g. Kuntschner 2000; Bernardi et al. 2003; Caldwell et al. 2003).

In order to compare our data with the literature, we choose two data sets which cover luminous early-type galaxies (González 1993; Trager et al. 2000, $(R_e/8)$ extractions) and fainter ones (Caldwell et al. 2003, global extractions). Our sample of 48 early-type galaxies shows good agreement with the literature for the $\text{H}\beta$, $\text{Mg } b$ and $\text{Fe}5270$ indices (see Fig. 17). For $\text{Fe}5015$, which was only observed by Caldwell et al. (2003), an offset of approximately 0.01 mag at intermediate velocity dispersions is visible, in the sense that our data have the larger values. The best-fitting linear index– σ relations for $\log \sigma \geq 2.1$, using errors in both variables, are given in Table 6.

There is no significant evidence for an environmental influence on the index– σ relations in our sample. However, it is generally the low-velocity dispersion S0s which show the strongest anticorrelation between $\text{H}\beta$ and metal line strengths. The reason for the scatter in the index– σ relations is typically ascribed to a combination of age, metallicity and abundance ratio variations at a given σ (e.g. Kuntschner et al. 2001; Thomas et al. 2005). We explore this further in a forthcoming paper in this series.

8 CONCLUDING REMARKS

The maps presented in this paper are the result of a comprehensive survey of the absorption line strength distributions of nearby early-type galaxies with an integral-field spectrograph. This data set demonstrates that many nearby early-type galaxies display a significant and varied structure in their line strength properties. This structure is sometimes very apparent as in the case of the post-starburst affected central regions of galaxies, or it can be of subtle nature as seen in the deviations of $\text{Mg } b$ isointensity contours compared to the isophotes of galaxies.

The two-dimensional coverage of the line strengths allows us to connect the stellar populations with the kinematical structure of the galaxies and thus improve our knowledge of the star formation and assembly history of early-type galaxies. For example, we find the $\text{Mg } b$ isointensity contours to be flatter than the isophotes for 18 galaxies which generally exhibit significant rotation. We infer from this that the rotational supported substructure features a higher metallicity and/or an increased Mg/Fe ratio as compared to the galaxy as a whole. Further steps in this direction will be presented in forthcoming papers of this series.

The metal line strength maps show generally negative gradients with increasing radius, while the $\text{H}\beta$ maps are typically flat or show

a mild positive outwards radial gradient. A few galaxies show strong central peaks and/or elevated overall $H\beta$ strength likely connected to recent star formation activity. For the most prominent post-starburst galaxies, even the metal line strength maps show a reversed gradient. We use the maps to compute average line strengths integrated over circular apertures of one-eighth effective radius. The resulting index versus velocity dispersion relations compare well with previous long-slit work.

ACKNOWLEDGMENTS

The SAURON project is made possible through grants 614.13.003, 781.74.203, 614.000.301 and 614.031.015 from the Netherlands Organization for Scientific Research (NWO) and financial contributions from the Institut National des Sciences de l'Univers, the Université Claude Bernard Lyon I, the Universities of Durham, Leiden, and Oxford, the British Council, PPARC grant 'Extragalactic Astronomy & Cosmology at Durham 1998–2002', and the Netherlands Research School for Astronomy NOVA. RLD is grateful for the award of a PPARC Senior Fellowship (PPA/Y/S/1999/00854) and postdoctoral support through PPARC grant PPA/G/S/2000/00729. The PPARC Visitors grant (PPA/V/S/2002/00553) to Oxford also supported this work. We are grateful to the Lorentz centre at university of Leiden for generous hospitality. MC acknowledges support from a VENI grant 639.041.203 awarded by the Netherlands Organization for Scientific Research. JFB acknowledges support from the Euro3D Research Training Network, funded by the EC under contract HPRN-CT-2002-00305. This project made use of the HyperLeda and NED data bases. Part of this work is based on data obtained from the ESO/ST-ECF Science Archive Facility. The SAURON team wishes to thank Emilie Jourdeuil for contributions in an early stage of this project.

REFERENCES

- Afanasiev V. L., Sil'chenko O. K., 2002, *AJ*, 124, 706
 Bacon R. et al., 2001, *MNRAS*, 326, 23 (Paper I)
 Bender R., Doebereiner S., Moellenhoff C., 1988, *A&AS*, 74, 385
 Bender R., Burstein D., Faber S. M., 1993, *ApJ*, 411, 153
 Bender R., Saglia R. P., Gerhard O. E., 1994, *MNRAS*, 269, 785
 Bernardi M. et al., 2003, *AJ*, 125, 1882
 Bica E., Alloin D., Schmidt A. A., 1990, *A&A*, 228, 23
 Bohlin R. C., Dickinson M. E., Calzetti D., 2001, *AJ*, 122, 2118
 Bower G. A. et al., 2000, *ApJ*, 534, 189
 Brodie J. P., Hanes D. A., 1986, *ApJ*, 300, 258
 Burbidge E. M., Burbidge G. R., 1959, *ApJ*, 130, 20
 Bureau M., Athanassoula E., 2005, *ApJ*, 626, 159
 Burstein D., Faber S. M., Gaskell C. M., Krumm N., 1984, *ApJ*, 287, 586
 Burstein D., Davies R. L., Dressler A., Faber S. M., Lynden-Bell D., 1988, in Kron R. G., Renzini A., eds, *ASSL Vol. 141. Towards Understanding Galaxies at High Redshift*. Kluwer, Dordrecht, p. 17
 Busarello G., Capaccioli M., D'Onofrio M., Longo G., Richter G., Zaggia S., 1996, *A&A*, 314, 32
 Caldwell N., Rose J. A., Concannon K. D., 2003, *AJ*, 125, 2891
 Capetti A., de Ruiter H. R., Fanti R., Morganti R., Parma P., Ulrich M.-H., 2000, *A&A*, 362, 871
 Cappellari M. et al., 2006, *MNRAS*, 366, 1126 (Paper IV)
 Cappellari M., Copin Y., 2003, *MNRAS*, 342, 345
 Cappellari M., Emsellem E., 2004, *PASP*, 116, 138
 Cardiel N., Gorgas J., Cenarro J., Gonzalez J. J., 1998, *A&AS*, 127, 597
 Carlberg R. G., 1984, *ApJ*, 286, 403
 Carollo C. M., Danziger I. J., Buson L., 1993, *MNRAS*, 265, 553
 Colless M., Burstein D., Davies R. L., McMahan R. K., Saglia R. P., Wegner G., 1999, *MNRAS*, 303, 813
 Davies R. L., Efstathiou G., Fall S. M., Illingworth G., Schechter P. L., 1983, *ApJ*, 266, 41
 Davies R. L., Sadler E. M., Peletier R. F., 1993, *MNRAS*, 262, 650
 de Zeeuw P. T. et al., 2002, *MNRAS*, 329, 513 (Paper II)
 del Burgo C., Peletier R. F., Vazdekis A., Arribas S., Mediavilla E., 2001, *MNRAS*, 321, 227
 Denicoló G., Terlevich R., Terlevich E., Forbes D. A., Terlevich A., Carrasco L., 2005, *MNRAS*, 356, 1440
 Efstathiou G., Ellis R. S., Carter D., 1980, *MNRAS*, 193, 931
 Efstathiou G., Ellis R. S., Carter D., 1982, *MNRAS*, 201, 975
 Emsellem E., Bacon R., Monnet G., Poulain P., 1996, *A&A*, 312, 777
 Emsellem E. et al., 2004, *MNRAS*, 352, 721 (Paper III)
 Faber S. M., 1973, *ApJ*, 179, 731
 Falcón-Barroso J. et al., 2004, *MNRAS*, 350, 35
 Falcón-Barroso J. et al., 2006, *MNRAS*, in press (doi:10.1111/j.1365-2966.2006.10261.x) (Paper VII, this issue)
 Fernandes R. C. et al., 2004, *ApJ*, 605, 105
 Fisher D., Franx M., Illingworth G., 1996, *ApJ*, 459, 110
 González J. J., 1993, PhD thesis, Univ. California at Santa Cruz
 Gonzalez J. J., Gorgas J., 1995, in Buzzoni A., Renzini A., Serrano A., eds, *ASP Conf. Ser., Vol. 86, Fresh Views of Elliptical Galaxies*. Astron. Soc. Pac., San Francisco, p. 225
 Gorgas J., Efstathiou G., Salamañca A. A., 1990, *MNRAS*, 245, 217
 Goudfrooij P., Hansen L., Jørgensen H. E., Norgaard-Nielsen H. U., 1994, *A&AS*, 105, 341
 Hau G. K. T., 1998, PhD thesis, Univ. Cambridge
 Ho L. C., Filippenko A. V., Sargent W. L. W., 1997, *ApJS*, 112, 315
 Jones L. A., 1997, PhD thesis, Univ. North Carolina
 Jørgensen I., 1999, *MNRAS*, 306, 607
 Jørgensen I., Franx M., Kjaergaard P., 1995, *MNRAS*, 276, 1341
 King D. L., 1985, Technical Note 31, Atmospheric Extinction at the Roque de los Muchachos Observatory, La Palma. The Royal Greenwich Observatory (RGO)
 Kobayashi C., Arimoto N., 1999, *ApJ*, 527, 573
 Korn A. J., Maraston C., Thomas D., 2005, *A&A*, 438, 685
 Kuntschner H., 2000, *MNRAS*, 315, 184
 Kuntschner H., 2004, *A&A*, 426, 737
 Kuntschner H., Lucey J. R., Smith R. J., Hudson M. J., Davies R. L., 2001, *MNRAS*, 323, 615
 McDermid R. M. et al., 2004, *Astron. Nachr.*, 325, 100
 McDermid R. M., Kuntschner H., Davies R. L., Vazdekis A., 2005, *MNRAS*, submitted
 Mehlert D., Saglia R. P., Bender R., Wegner G., 2000, *A&AS*, 141, 449
 Mehlert D., Thomas D., Saglia R. P., Bender R., Wegner G., 2003, *A&A*, 407, 423
 Michard R., 1999, *A&AS*, 137, 245
 Michard R., Simien F., 1988, *A&AS*, 74, 25
 Morelli L. et al., 2004, *MNRAS*, 354, 753
 Norris M. A., Sharples R. M., Kuntschner H., 2006, *MNRAS*, 367, 815
 Peletier R. F., Davies R. L., Illingworth G. D., Davis L. E., Cawson M., 1990, *AJ*, 100, 1091
 Peletier R. F., Christodoulou D. M., 1993, *AJ*, 105, 1378
 Peletier R. F., Balcells M., Davies R. L., Andredakis Y., Vazdekis A., Burkert A., Prada F., 1999, *MNRAS*, 310, 703
 Peletier R. F., Vazdekis A., Arribas S., del Burgo C., García-Lorenzo B., Gutiérrez C., Mediavilla E., Prada F., 1999, *MNRAS*, 310, 863
 Peng C. Y., Ho L. C., Impey C. D., Rix H., 2002, *AJ*, 124, 266
 Proctor R. N., Sansom A. E., 2002, *MNRAS*, 333, 517
 Quillen A. C., Bower G. A., Stritzinger M., 2000, *ApJS*, 128, 85
 Rampazzo R., Annibali F., Bressan A., Longhetti M., Padoan F., Zeilinger W. W., 2005, *A&A*, 433, 497
 Rix H., Franx M., Fisher D., Illingworth G., 1992, *ApJ*, 400, L5
 Rose J. A., 1985, *AJ*, 90, 1927
 Sánchez-Blázquez P., 2004, PhD thesis, Universidad Complutense, Madrid
 Sarzi M. et al., 2006, *MNRAS*, 366, 1151 (Paper V)
 Sarzi M., Rix H., Shields J. C., Rudnick G., Ho L. C., McIntosh D. H., Filippenko A. V., Sargent W. L. W., 2001, *ApJ*, 550, 65
 Sil'chenko O. K., 2005, *Astron. Lett.*, 31, 227

- Sil'chenko O. K., Afanasiev V. L., Chavushyan V. H., Valdes J. R., 2002, *ApJ*, 577, 668
- Sil'chenko O. K., Moiseev A. V., Afanasiev V. L., Chavushyan V. H., Valdes J. R., 2003, *ApJ*, 591, 185
- Terlevich R., Davies R. L., Faber S. M., Burstein D., 1981, *MNRAS*, 196, 381
- Thomas D., Maraston C., Bender R., 2003, *MNRAS*, 339, 897
- Thomas D., Maraston C., Bender R., de Oliveira C. M., 2005, *ApJ*, 621, 673
- Trager S. C., Faber S. M., Worthey G., González J. J., 2000, *AJ*, 119, 1645
- Trager S. C., Worthey G., Faber S. M., Burstein D., Gonzalez J. J., 1998, *ApJS*, 116, 1
- Turnbull A. J., Bridges T. J., Carter D., 1999, *MNRAS*, 307, 967
- van den Bosch F. C., Emsellem E., 1998, *MNRAS*, 298, 267
- Vazdekis A., 1999, *ApJ*, 513, 224
- Wagner S. J., Bender R., Moellenhoff C., 1988, *A&A*, 195, L5
- Wernli F., Emsellem E., Copin Y., 2002, *A&A*, 396, 73
- White S. D. M., 1980, *MNRAS*, 191, 1P
- Worthey G., 1994, *ApJS*, 95, 107
- Worthey G., Collobert M., 2003, *ApJ*, 586, 17
- Worthey G., Faber S. M., Gonzalez J. J., 1992, *ApJ*, 398, 69
- Worthey G., Faber S. M., Gonzalez J. J., Burstein D., 1994, *ApJS*, 94, 687
- Worthey G., Ottaviani D. L., 1997, *ApJS*, 111, 377

APPENDIX A: DESCRIPTION FOR INDIVIDUAL GALAXIES

Here, we briefly comment on the line strength structures observed in the SAURON maps of the E/S0 sample presented in this paper. Individual comments on the stellar kinematics and the emission-line maps are presented in Papers III and V, respectively. A thorough and quantitative assessment of the line strength maps with the help of stellar population models will be carried out in subsequent papers. Independently derived line strength maps for NGC 524, 1023 3379, 3384, 4550, 7332 and 7457 based on our observations were presented and discussed in Afanasiev & Sil'chenko (2002), Sil'chenko et al. (2002, 2003) and Sil'chenko (2005).

NGC 474. This galaxy (Arp 227), famous for its shell structures (e.g. Turnbull, Bridges & Carter 1999), shows normal metal line strength gradients. The $H\beta$ map appears relatively flat in the inner regions, while we observe rising $H\beta$ strength towards larger radii.

NGC 524. This galaxy shows regular $Mg\ b$ gradients, and the $H\beta$ map shows a mild positive gradient. The two Fe maps show a noisy structure which may partly be caused by low S/N in the outer bins.

NGC 821. A close to edge-on galaxy with a rapidly rotating disc-like component (see Paper III) shows an enhanced core region in all metal line maps. There is also evidence for the $Mg\ b$ contours to be flatter than the isophotes. The $H\beta$ map appears rather featureless (see also McDermid et al. 2005). The maps are consistent with the results from long-slit spectroscopy of Sánchez-Blázquez (2004).

NGC 1023. This SB0 galaxy, with a prominent twist in the central velocity field (see Paper III), shows a central concentration in all metal lines. The metal line strength at larger radii appears flat and even tend to rise again at the edges of the FoV. The $H\beta$ map is consistent with a constant value over the full FoV.

NGC 2549. This galaxy with a thin, rapidly rotating component (see Paper III) shows enhanced Fe5015 and Fe5270_s strength along this component. The $H\beta$ line strength is also elevated in the central regions.

NGC 2685. This famous object, the Helix galaxy (Burbidge & Burbidge 1959; Peletier & Christodoulou 1993), shows significant extinction due to polar dust lanes on its north-east side. The $H\beta$ map shows enhanced values over large regions of the FoV, while the metal line strength maps are elevated along the rotation direction.

NGC 2695. The metal line strength maps show normal gradients consistent with the isophotes. The $H\beta$ map is flat, however, at notably low values.

NGC 2699. This galaxy shows regular metal line strength gradients consistent with the isophotes. The $H\beta$ map is relatively flat at a slightly elevated level compared to the bulk of the objects in our sample.

NGC 2768. This galaxy with a rather cylindrical velocity field shows regular metal line strength gradients. The $H\beta$ map appears rather flat. Significant dust extinction is present north of the centre (Michard 1999).

NGC 2974. This rapidly rotating galaxy shows evidence of enhanced metal line strength along the rotation direction. The $H\beta$ map appears relatively flat. The long-slit observations of Rampazzo et al. (2005) show declining $H\beta$ strength with radius while Carollo et al. (1993) data suggest a modest increase with radius. Our emission-line maps (Paper V) show significant [O III] and $H\beta$ emission basically over the full FoV, and thus different $H\beta$ emission corrections are likely the cause of the literature disagreement on $H\beta$ absorption strengths.

NGC 3032. This dusty galaxy shows negative $Mg\ b$ and Fe5270_s line strength gradients. The Fe5015 map shows a ring-like structure of weak absorption while the centre exhibits strong Fe5015 absorption. The $H\beta$ map reveals a prominent peak in the centre and shows evidence of rising values at larger radii. The unusual structure of the line strength maps and the relatively strong emission detected in this galaxy (see Fig. 6 and Paper V) suggest that a recent starburst has occurred in this galaxy with weak evidence of ongoing star formation.

NGC 3156. Another dusty galaxy with negative $Mg\ b$ line strength gradients in the centre. The Fe5015 and Fe5270_s maps do not show a clear structure. The $H\beta$ map exhibits a strong peak in the centre with a gradual decline to the outskirts. The line strength maps suggest a post-starburst scenario for this galaxy (see also Denicoló et al. 2005).

NGC 3377. This discy galaxy (Bender et al. 1988; Michard & Simien 1988) shows metal line strengths which are more flattened than the isophotes. Conversely, the $H\beta$ absorption has a rather constant moderate value across the field. The line strength maps are consistent with Sánchez-Blázquez (2004).

NGC 3379 (M105). This rather round object shows normal metal line strengths gradients consistent with the isophotes. The $H\beta$ map shows weakly increasing line strength towards larger radii, as found by other authors (e.g. Davies et al. 1993; Sánchez-Blázquez 2004, see also Fig. 4).

NGC 3384. This SB0 galaxy shows a dynamically cold component in the central 5 arcsec (see Paper III), which may correspond to the red major axis disc component found by (Busarello et al. 1996). The line strength indices have already been presented in Paper II. The metal line strengths show regular gradients consistent with the isophotes. The $H\beta$ absorption map, at moderately elevated values (see also Kuntschner et al. 2001), appears flat in the inner regions with weak evidence for increasing $H\beta$ strength at large radii.

NGC 3414. This disturbed galaxy (Arp 162) contains a kinematically decoupled component (hereafter KDC; see Paper III) within the central 10 arcsec. The line strength maps appear to have regular gradients.

NGC 3489. This dusty galaxy shows a fast-rotating central component and a complex morphology of the odd higher order kinematic moment h_3 (see Paper III). The $H\beta$ absorption strength is globally high (see also Kuntschner et al. 2001; Rampazzo et al. 2005), with

a sharp central (2 arcsec) enhancement, also evident with OASIS (McDermid et al. 2004).

NGC 3608. This galaxy shows a kinematically decoupled core (Paper III and references therein) extending to around 13 arcsec. Our metal line strengths appear more flattened than the isophotes within this region. The $H\beta$ absorption map shows a mild positive gradient with radius. Line strength are consistent with Sánchez-Blázquez (2004).

NGC 4150. Notable obscuration from dust is visible in the central parts of this galaxy (Quillen, Bower & Stritzinger 2000). A KDC resides in the central few arcsec of this galaxy (see Paper III), coincident with a strong drop in the $Mg\ b$ absorption strength and a corresponding peak in $H\beta$ absorption strength, which itself is globally enhanced. The iron line maps are relatively featureless by comparison, with no strong central features. The core is therefore dominated by a young stellar population, as found by other authors (e.g. Fernandes et al. 2004).

NGC 4262. This strongly barred object shows inconspicuous metal line gradients. The $H\beta$ absorption map shows a mild increase with radius.

NGC 4270. The central peaked metal absorption line strengths in this galaxy show evidence of an increase beyond 10 arcsec along the major axis, giving a small dip around 4–5 arcsec from the centre. The $H\beta$ absorption map shows no significant features.

NGC 4278. This LINER (Ho, Filippenko & Sargent 1997) and radio source (e.g. Capetti et al. 2000) show some central dust features (e.g. Peng et al. 2002). There is some evidence that the $Mg\ b$ contours are more flattened than the isophotes. There is a well-defined depression in the $H\beta$ line strength within the central 5 arcsec (see also Davies et al. 1993) which we partly ascribe to imperfect removal of strong $H\beta$ emission.

NGC 4374 (M84). This well-known giant elliptical shows notable dust absorption (Quillen et al. 2000) and has a BL Lac nucleus (Bower et al. 2000). The metal lines have a similar morphology to those in NGC 4278, following the isophotes in general. The $H\beta$ absorption map is rather flat, showing a slight increase towards the edge of the field, also present in the data of Davies et al. (1993), Carollo et al. (1993) and Sánchez-Blázquez (2004).

NGC 4382 (M85). This well-known object shows a distinct depression in $Mg\ b$ within the central 10 arcsec, consistent with Fisher et al. (1996), which appears slightly more flattened than the isophotes. This is coincident with an enhancement in the $H\beta$ absorption map (see also Kuntschner et al. 2001), as well as corresponding closely to a region of peculiar kinematic behaviour (decoupled rotation, low-velocity dispersion, and complex higher order terms—see Paper III). There is also evidence for a flattened feature in the iron absorption maps within this region, most evident in the Fe5015 map.

NGC 4387. This boxy galaxy (Peletier et al. 1990) shows regular metal line gradients consistent with the isophotes. The $H\beta$ map appears relatively flat in the inner regions while we observe a drop of $H\beta$ strength towards larger radii.

NGC 4458. This galaxy with a KDC (see Paper III) shows line strength gradients consistent with the isophotes. The region of the KDC is inconspicuous in the $H\beta$ map (see also Morelli et al. 2004).

NGC 4459. This galaxy shows a central region of stronger $H\beta$ absorption with a ring-like structure around it. This is consistent with the central dust ring found in this galaxy (see Paper V and Sarzi et al. 2001). The metal lines show relatively regular gradients.

NGC 4473. This galaxy exhibits a complex morphology in the velocity dispersion map, with a region of high dispersion along the major axis which widens at larger radii, which probably corresponds to two counter-rotating stellar discs. The metal line strength maps

are more flattened than the isophotes, indicating a higher metallicity in the disc(s), while the $H\beta$ map is rather flat.

NGC 4477. This galaxy shows a prominent misalignment of the kinematic and photometric major axis. The metal line strength maps show an inner region with enhanced metallicity and show little structure elsewhere. There is weak evidence at larger radii along the major axis for increased metal line strength. The $H\beta$ map appears flat.

NGC 4486. The line strength in the central 3 arcsec and some part of the jet region of this famous Virgo galaxy are clearly affected by an imperfect removal of emission lines and non-thermal emission (Davies et al. 1993). Overall, the line strength maps appear flat over large parts of the FoV. The $H\beta$ map exhibits notably low values.

NGC 4526. This S0 object has a prominent dust disc which is not only visible in the reconstructed SAURON image but also clearly seen in the $Mg\ b$ and $H\beta$ maps. The strong $H\beta$ line strengths in the region of the dust lane indicate the presence of dust enshrouded young stars.

NGC 4546. This galaxy exhibits ionized gas counter-rotating with respect to the stars (see Paper V). The $Mg\ b$ contours are more elongated in the direction of the rotation than the isophotes. This effect is less prominent in the iron maps. The $H\beta$ map appears relatively flat with a hint of weaker $H\beta$ absorption along the major axis.

NGC 4550. This S0 galaxy has two counter-rotating stellar discs of similar mass (Rix et al. 1992). There is evidence for the $Mg\ b$ contours being flatter than the isophotes. The $H\beta$ map shows a mildly elevated level in the central region along the major axis.

NGC 4552. This large elliptical shows regular line strength gradients, consistent with Sánchez-Blázquez (2004) and Rampazzo et al. (2005). The $H\beta$ map appears flat and shows notably low values.

NGC 4564. This highly elongated galaxy shows isoindex contours of the $Mg\ b$ and the Fe indices which are more flattened than the isophotes, indicating that the bulge and disc of this galaxy have different stellar populations.

NGC 4570. This edge-on S0 galaxy features multiple kinematic components such as an outer and a nuclear disc (van den Bosch & Emsellem 1998). The $Mg\ b$ map and to a lesser extent the Fe maps show a central peak surrounded by a region depressed in line strength. At larger radii, the onset of the outer disc, showing strong metal lines, can be seen. The $H\beta$ map is relatively flat.

NGC 4621. This is another object with a strong indication from the stellar kinematics of a disc component, which is also seen in the metal line strength maps showing more flattened isoindex contours than the isophotes. The inner 60 pc harbour a counter-rotating core (Wernli, Emsellem & Copin 2002). The $H\beta$ map appears relatively flat.

NGC 4660. Similar to NGC 4621, there are strong indications for a disc component in this galaxy, accompanied by pointy discy isophotes. This galaxy is among the best examples of $Mg\ b$ isoindex contours to be flatter than the isophotes for galaxies with strong rotation.

NGC 5198. This galaxy, with a central KDC, rotating nearly perpendicularly to the outer body, shows regular metal line gradients and a mild positive $H\beta$ gradient.

NGC 5308. This is a typical case of a close to edge-on disc galaxy showing a rapidly rotating component (Paper III) and a double sign reversal in h_3 , indicating a central bar (Bureau & Athanassoula 2005). The metal line strength gradients are regular and appear to be consistent with the isophotes.

NGC 5813. A galaxy with a well-known KDC (Efsthathiou, Ellis & Carter 1980, 1982; Bender, Saglia & Gerhard 1994, Paper III). The line strength maps of this galaxy have already been presented

in Paper II. Here, it is shown that we reproduce the large $Mg\,b$ gradient presented by Gorgas et al. (1990). The KDC is not seen in the absorption line maps.

NGC 5831. The kinematics of this galaxy reveal the presence of a well-known KDC (Davies et al. 1983; Peletier et al. 1990, Paper III). The KDC is not really seen in the line strength maps, apart from the $Mg\,b$ map which appears to be more elongated in the direction of the KDC than the isophotes. The $H\beta$ map appears relatively flat.

NGC 5838. This boxy galaxy is a strong rotator and Peletier et al. (1990) show that the bulge of this galaxy contains old stellar populations with small colour gradients, except for the inner 2 arcsec. This is consistent with our line strength maps which show regular gradients and a mild peak of the $H\beta$ map in the very centre. There is evidence for the $Mg\,b$ contours being flatter than the isophotes. Our emission-line maps (see Paper V) also show significant detection in the centre with evidence for a rotating structure.

NGC 5845. This galaxy is a compact elliptical, close to NGC 5846. Small gradients in the line strength maps are seen, consistent with Sánchez-Blázquez (2004). The central disc, clearly seen in the stellar kinematics (Paper III), is not apparent in the line strength maps.

NGC 5846. The SAURON FoV of this bright giant elliptical includes a foreground star and a companion (NGC 5846A) north and

south of its nucleus, respectively. The line strength maps are generally regular, with small gradients. The line strengths are consistent with Sánchez-Blázquez (2004) and Rampazzo et al. (2005).

NGC 5982. For this galaxy, we confirm the presence of a KDC first detected by Wagner, Bender & Moellenhoff (1988). The KDC is not clearly seen in the line strength maps; however, there is evidence for the $Mg\,b$ contours being flatter than the isophotes. The $H\beta$ map appears relatively flat.

NGC 7332. Another strongly boxy galaxy with a KDC (counter-rotating) in the central 3 arcsec (see Falcón-Barroso et al. 2004). There is evidence for the $Mg\,b$ contours being flatter than the isophotes. The galaxy shows high $H\beta$ values, indicating an age of about 3 Gyr (see Falcón-Barroso et al. 2004). The data are consistent with Sánchez-Blázquez (2004) and Rampazzo et al. (2005).

NGC 7457. This small S0 galaxy with a KDC shows surprisingly little structure in its line strength maps, consistent with the colour profiles of Peletier et al. (1999). The high $H\beta$ values indicate a relatively young age.

This paper has been typeset from a $\mathrm{T}_{\mathrm{E}}\mathrm{X}/\mathrm{L}^{\mathrm{A}}\mathrm{T}_{\mathrm{E}}\mathrm{X}$ file prepared by the author.